Mon. Not. R. Astron. Soc. **382,** 29–47 (2007) doi:10.1111/j.1365-2966.2007.12275.x

The Bullet Cluster 1E0657-558 evidence shows modified gravity in the absence of dark matter

J. R. Brownstein[1⋆] and J. W. Moffat[2⋆]

[1]*Perimeter Institute for Theoretical Physics, Waterloo, Ontario N2L 2Y5, Canada*
[2]*Department of Physics & Astronomy, University of Waterloo, Waterloo, Ontario N2L 3G1, Canada*

Accepted 2007 July 26. Received 2007 June 18; in original form 2007 February 20

ABSTRACT

A detailed analysis of the 2006 November 15 data release X-ray surface density Σ-map and the strong and weak gravitational lensing convergence κ-map for the Bullet Cluster 1E0657-558 is performed and the results are compared with the predictions of a modified gravity (MOG) and dark matter. Our surface density Σ-model is computed using a King β-model density, and a mass profile of the main cluster and an isothermal temperature profile are determined by the MOG. We find that the main cluster thermal profile is nearly isothermal. The MOG prediction of the isothermal temperature of the main cluster is $T = 15.5 \pm 3.9$ keV, in good agreement with the experimental value $T = 14.8^{+2.0}_{-1.7}$ keV. Excellent fits to the 2D convergence κ-map data are obtained without non-baryonic dark matter, accounting for the 8σ spatial offset between the Σ-map and the κ-map reported in Clowe et al. The MOG prediction for the κ-map results in two baryonic components distributed across the Bullet Cluster 1E0657-558 with averaged mass fraction of 83 per cent intracluster medium (ICM) gas and 17 per cent galaxies. Conversely, the Newtonian dark matter κ-model has on average 76 per cent dark matter (neglecting the indeterminant contribution due to the galaxies) and 24 per cent ICM gas for a baryon to dark matter mass fraction of 0.32, a statistically significant result when compared to the predicted Λ-cold dark matter cosmological baryon mass fraction of $0.176^{+0.019}_{-0.012}$.

Key words: gravitation – gravitational lensing – galaxies: clusters: individual: 1E0657-558 – dark matter – X-rays: individual: 1E0657-558.

1 INTRODUCTION

1.1 The question of missing mass

Galaxy cluster masses have been known to require some form of energy density that makes its presence felt only by its gravitational effects since Zwicky (1933) analysed the velocity dispersion for the Coma cluster. Application of the Newtonian $1/r^2$ gravitational force law inevitably points to the question of missing mass, and may be explained by dark matter (Oort 1932). The amount of non-baryonic dark matter required to maintain consistency with Newtonian physics increases as the mass scale increases so that the mass-to-light ratio of clusters of galaxies exceeds the mass-to-light ratio for individual galaxies by as much as a factor of $\sim$6, which exceeds the mass-to-light ratio for the luminous inner core of galaxies by as much as a factor of $\sim$10. In clusters of galaxies, the dark matter paradigm leads to a mass-to-light ratio as much as $300\,M_\odot/L_\odot$. In this scenario, non-baryonic dark matter dominates over baryons outside the cores of galaxies (by $\approx$80–90 per cent).

⋆E-mail: jbrownstein@perimeterinsitute.ca; john.moffat@utoronto.ca

Dark matter has dominated cosmology for the last five decades, although the search for dark matter has to this point come up empty. Regardless, one of the triumphs of cosmology has been the precise determination of the standard (power-law flat, ΛCDM) cosmological model parameters. The highly anticipated third-year results from the *Wilkinson Microwave Anisotropy Probe* team have determined the cosmological baryon mass fraction (to non-baryonic dark matter) to be $0.176^{+0.019}_{-0.012}$ (Spergel et al. 2006). This ratio may be inverted, so that for every gram of baryonic matter, there are 5.68 grams of non-baryonic dark matter – at least on cosmological scales. There seems to be no evidence of dark matter on the scale of the Solar system, and the cores of galaxies also seem to be devoid of dark matter.

Galaxy clusters and superclusters are the largest virialized (gravitationally bound) objects in the Universe and make ideal laboratories for gravitational physicists. The data come from three sources:

(i) X-ray imaging of the hot intracluster medium (ICM).
(ii) Hubble, *Spitzer* and Magellan telescope images of the galaxies comprising the clusters.
(iii) strong and weak gravitational lensing surveys which may be used to calculate the mass distribution projected on to the sky (within a particular theory of gravity).

The alternative to the dark matter paradigm is to modify the Newtonian $1/r^2$ gravitational force law so that the ordinary (visible) baryonic matter accounts for the observed gravitational effect. An analysis of the Bullet Cluster 1E0657-558 surface density Σ-map and convergence κ-map data by Angus, Famaey & Zhao (2006) and Angus et al. (2007) based on Milgrom's Modified Newtonian Dynamics (MOND) model (Milgrom 1983; Sanders & McGaugh 2002) and Bekenstein's relativistic version of MOND (Bekenstein 2004) failed to fit the data without dark matter. More recently, further evidence that MOND needs dark matter in weak lensing of clusters has been obtained by Takahashi & Chiba (2007). Problems with fitting X-ray temperature profiles with Milgrom's MOND model without dark matter were shown in Aguirre, Schaye & Quataert (2001), Sanders (2006), Pointecouteau & Silk (2005) and Brownstein & Moffat (2006b). Neutrino matter with an electron neutrino mass $m_\nu \sim 2\,\mathrm{eV}$ can fit the Bullet Cluster data (Angus et al. 2006, 2007; Sanders 2006). This mass is at the upper bound obtained from observations. The Karlsruhe Tritium Neutrino (KATRIN) experiment will be able to falsify 2 eV electron neutrinos at 95 per cent confidence level within months of taking data in 2009.

The theory of modified gravity – or MOG model – based on a covariant generalization of Einstein's theory with auxiliary (gravitational) fields in addition to the metric was proposed in Moffat (2005, 2006a) including metric–skew–tensor gravity (MSTG) theory and scalar–tensor–vector gravity (STVG) theory. Both versions of MOG, MSTG and STVG modify the Newtonian $1/r^2$ gravitational force law in the same way so that it is valid at small distances, say at terrestrial scales.

Brownstein & Moffat (2006a) applied MOG to the question of galaxy rotation curves, and presented the fits to a large sample of over 100 low surface brightness (LSB), high surface brightness (HSB) and dwarf galaxies. Each galaxy rotation curve was fit without dark matter using only the available photometric data (stellar matter and visible gas) and alternatively a two-parameter mass distribution model which made no assumption regarding the mass-to-light ratio. The results were compared to MOND and were nearly indistinguishably right out to the edge of the rotation curve data, where MOND predicts a forever flat rotation curve, but MOG predicts an eventual return to the familiar $1/r^2$ gravitational force law. The mass-to-light ratio varied between 2 and $5\,\mathrm{M}_\odot/\mathrm{L}_\odot$ across the sample of 101 galaxies in contradiction to the dark matter paradigm which predicts a mass-to-light ratio typically as high as $50\,\mathrm{M}_\odot/\mathrm{L}_\odot$.

In a sequel, Brownstein & Moffat (2006b) applied MOG to the question of galaxy cluster masses, and presented the fits to a large sample of over 100 X-ray galaxy clusters of temperatures ranging from 0.52 keV (six million kelvin) to 13.29 keV (150 million kelvin). For each of the 106 galaxy clusters, the MOG provided a parameter-free prediction for the ICM gas mass profile, which reasonably matched the X-ray observations (King β-model) for the same sample compiled by Reiprich (2001) and Reiprich & Böhringer (2002). The MOND predictions were presented for each galaxy cluster, but failed to fit the data. The Newtonian dark matter result outweighed the visible ICM gas mass profiles by an order of magnitude.

In the Solar system, the Doppler data from the Pioneer 10 and 11 spacecraft suggest a deviation from the Newtonian $1/r^2$ gravitational force law beyond Saturn's orbit. Brownstein & Moffat (2006c) applied MOG to fit the available anomalous acceleration data (Nieto & Anderson 2005) for the Pioneer 10/11 spacecraft. The solution showed a remarkably low variance of residuals corresponding to a reduced χ^2 per degree of freedom of 0.42, signalling a good fit. The magnitude of the satellite acceleration exceeds the MOND critical acceleration, negating the MOND solution (Sanders 2006). The dark matter paradigm is severely limited within the Solar system by stability issues of the Sun, and precision gravitational experiments including satellite, lunar laser ranging and measurements of the Gaussian gravitational constant and Kepler's law of planetary motion. Without an actual theory of dark matter, no attempt to fit the Pioneer anomaly with dark matter has been suggested. Remarkably, MOG provides a closely fit solution to the Pioneer 10/11 anomaly and is consistent with the accurate equivalence principle, all current satellite, laser ranging observations for the inner planets and the precession of perihelion for all of the planets.

A fit to the acoustical wave peaks observed in the cosmic microwave background (CMB) data using MOG has been achieved without dark matter. Moreover, a possible explanation for the accelerated expansion of the Universe has been obtained in MOG (Moffat 2007).

Presently, on both an empirical and theoretical level, MOG is the most successful alternative to dark matter. The successful application of MOG across scales ranging from clusters of galaxies (Mpc) to HSB, LSB and dwarf galaxies (kpc), to the Solar system (au) provides a clue to the question of missing mass. The apparent necessity of the dark matter paradigm may be an artefact of applying the Newtonian $1/r^2$ gravitational force law to scales where it is not valid, where a theory such as MOG takes over. The 'excess gravity' that MOG accounts for may have nothing to do with the hypothesized missing mass of dark matter. But how can we distinguish the two? In most observable systems, gravity creates a central potential, where the baryon density is naturally the highest. So in most situations, the matter which is creating the gravity potential occupies the same volume as the visible matter. Clowe et al. (2006b) describe this as a degeneracy between whether gravity comes from dark matter or from the observed baryonic mass of the hot ICM and visible galaxies where the excess gravity is due to MOG. This degeneracy may be split by examining a system that is out of steady state, where there is spatial separation between the hot ICM and visible galaxies. This is precisely the case in galaxy cluster mergers: the galaxies will experience a different gravitational potential created by the hot ICM than if they were concentrated at the centre of the ICM. Moffat (2006b) considered the possibility that MOG may provide the explanation of the recently reported 'extra gravity' without non-baryonic dark matter which has so far been interpreted as direct evidence of dark matter. The research presented here addresses the full-sky data product for the Bullet Cluster 1E0657-558, recently released to the public (Clowe et al. 2006c).

1.2 The latest results from the Bullet Cluster 1E0657-558

(i) The *Chandra* Peer Review has declared the Bullet Cluster 1E0657-558 to be the most interesting cluster in the sky. This system, located at a redshift $z = 0.296$, has the highest X-ray luminosity and temperature ($T = 14.1 \pm 0.2\,\mathrm{keV}$, $\sim 1.65 \times 10^8\,\mathrm{K}$), and demonstrates a spectacular merger in the plane of the sky exhibiting a supersonic shock front, with Mach number as high as 3.0 ± 0.4 (Markevitch 2006). The Bullet Cluster 1E0657-558 has provided a rich data set in the X-ray spectrum which has been modelled to high precision. From the extra long 5.2×10^5 s *Chandra* space satellite X-ray image, the surface mass density, $\Sigma(x, y)$, was reconstructed providing a high-resolution map of the ICM gas (Clowe et al. 2006b). The Σ-map, shown in a false colour composite map (in red) in Fig. 1, is the result of a normalized geometric mass model based on a 16×16 arcmin field in the plane of the sky that covers the entire cluster and is composed of a square grid of 185×185 pixels

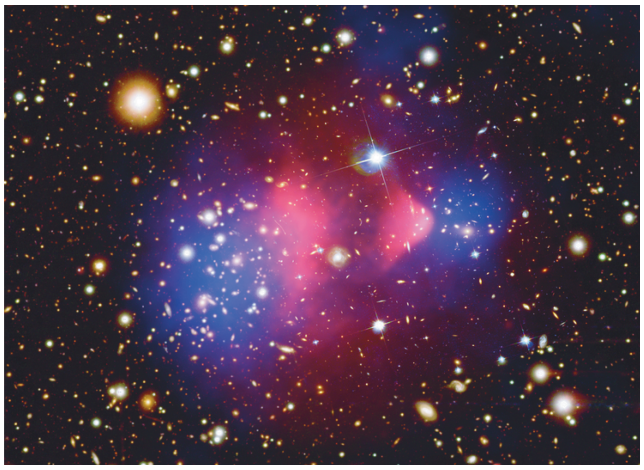

Figure 1. False colour image of Bullet Cluster 1E0657-558. The surface density Σ-map reconstructed from X-ray imaging observations is shown in red and the convergence κ-map as reconstructed from strong and weak gravitational lensing observations is shown in blue. Image provided courtesy of *Chandra* X-ray Observatory.

(∼8000 data points).[1] Our analysis of the Σ-map provides first published results for the King β-model density, as shown in Table 2, and mass profiles of the main cluster and the isothermal temperature profile as determined by MOG, as shown in Fig. 9.

(ii) Based on observations made with the NASA/ESA *Hubble Space Telescope* (*HST*), the *Spitzer Space Telescope* and the 6.5-m Magellan telescopes, Clowe et al. (2006a), Bradač et al. (2006) and Clowe et al. (2006b) report on a combined strong and weak gravitational lensing survey used to reconstruct a high-resolution, absolutely calibrated convergence κ-map of the region of sky surrounding Bullet Cluster 1E0657-558, without assumptions on the underlying gravitational potential. The κ-map is shown in the false colour composite map (in blue) in Fig. 1. The gravitational lensing reconstruction of the convergence map is a remarkable result, considering it is based on a catalogue of strong and weak lensing events and relies on a thorough understanding of the distances involved – ranging from the redshift of the Bullet Cluster 1E0657-558 ($z = 0.296$) which puts it at a distance of the order of one billion parsec away. Additionally, the typical angular diameter distances to the lensing event sources ($z \sim 0.8$ to $\sim$1.0) are several billion parsec distant! This is perhaps the greatest source of error in the κ-map which limits its precision. Regardless, we are able to learn much about the convergence map and its peaks.

Both the Σ-map and the κ-map are 2D distributions based on line-of-sight integration. We are fortunate, indeed, that the Bullet Cluster 1E0657-558 is not only one of the hottest, most supersonic, most massive cluster mergers seen, but the plane of the merger is also aligned with our sky! As exhibited in Fig. 1, the latest results from the Bullet Cluster 1E0657-558 show, beyond a shadow of doubt, that the Σ-map, which is a direct measure of the hot ICM gas, is offset from the κ-map, which is a direct measure of the curvature (convergence) of space–time. The fact that the κ-map is centred on the galaxies, and not on the ICM gas mass, is certainly evidence of either 'missing mass', as in the case of the dark matter paradigm, or 'extra gravity', as in the case of MOG. Clowe et al. (2006b) state "one would expect that this (the offset Σ- and κ-peaks) indicates that dark matter must be present regardless of the gravitational force law, but in some alternative gravity models, the multiple peaks can alter the lensing surface potential so that the strength of the peaks is no longer directly related to the matter density in them. As such, all of the alternative gravity models have to be tested individually against the observations."

The data from the Bullet Cluster 1E0657-558 provide a laboratory of the greatest scale, where the degeneracy between 'missing mass' and 'extra gravity' may be distinguished. We demonstrate that in MOG, the convergence κ-map correctly accounts for all of the baryons in each of the main and subclusters, including all of the galaxies in the regions near the main central dominant (CD) and the subcluster's brightest central galaxy (BCG), without non-baryonic dark matter.

1.3 How MOG may account for the Bullet Cluster 1E0657-558 evidence

We will show how MOG may account for the Bullet Cluster 1E0657-558 evidence, without dominant dark matter, by deriving the modifications to the gravitational lensing equations from MOG. Concurrently, we will provide comparisons to the equivalent Einstein–Newton results utilizing dark matter to explain the missing mass. The paper is divided as follows.

Section 2 is dedicated to the theory used to perform all of the derivations and numerical computations and is separated into three pieces: Section 2.1 presents the Poisson equations in MOG for a non-spherical distribution of matter and the corresponding derivation of the acceleration law and the dimensionless gravitational coupling, $\mathcal{G}$. Section 2.2 presents the King β-model density profile, ρ. Section 2.3 presents the derivation of the weighted surface mass density, $\bar{\Sigma} = \int \mathcal{G}\rho$, from the convergence $\kappa = \bar{\Sigma}/\Sigma_c$. The effect of the dimensionless gravitational coupling, $\mathcal{G}$, is to carry more weight away from the centre of the system. If the galaxies occur away from the centre of the ICM gas, as in the Bullet Cluster 1E0657-558, their contribution to the κ-map will be weighted by as much as a factor of 6 as shown in Fig. 7.

Section 3 is dedicated to the surface density Σ-map from the X-ray imaging observations of the Bullet Cluster 1E0657-558 from the 2006 November 15 data release Σ-map (Clowe et al. 2006c). Section 3.1 presents a visualization of the Σ-map and our low χ^2 best-fitting King β-model (neglecting the subcluster). Section 3.2 presents a determination of $\mathcal{G}$ for the Bullet Cluster 1E0657-558 based on the (>100) galaxy cluster survey of Brownstein & Moffat (2006b). Section 3.3 presents the cylindrical mass profile, $\int \Sigma$, about the main cluster Σ-map peak. Section 3.4 presents the isothermal spherical mass profile from which we have derived a parameter-free (unique) prediction for the X-ray temperature of the Bullet Cluster 1E0657-558 of $T = 15.5 \pm 3.9$ keV which agrees with the experimental value of $T = 14.8^{+2.0}_{-1.7}$ keV, within the uncertainty. Section 3.5 presents the details of the separation of the Σ-map into the main cluster and subcluster components.

Section 4 is dedicated to the convergence κ-map from the weak and strong gravitational lensing survey of the Bullet Cluster 1E0657-558 from the 2006 November 15 data release κ-map (Clowe et al. 2006c). Section 4.1 presents a visualization of the κ-map and some remarks on the evidence for dark matter or conversely, extra gravity. Section 4.2 presents the MOG solution which uses a projective approximation for the density profile to facilitate numerical integration, although the full non-spherically symmetric expressions are provided in Section 2.1. To a zeroth-order approximation, we present the spherically symmetric solution, which does not fit the Bullet Cluster 1E0657-558. In our next approximation, the

[1] Technical details are in Markevitch et al. (in preparation).

density profile of the Bullet Cluster 1E0657-558, ρ, is taken as the best-fitting King β-model (spherically symmetric), but the dimensionless gravitational coupling, $\mathcal{G}$, also assumed to be spherically symmetric, has a different centre – in the direction closer to the subcluster. We determined that our best-fitting κ-model corresponds to a location of the MOG centre 140 kpc away from the main cluster Σ-map towards the subcluster Σ-map peak. Section 4.3 presents the MOG prediction of the galaxy surface mass density, computed by taking the difference between the κ-map data and our κ-model of the Σ-map (ICM gas) data. 4.4 presents the mass profile of dark matter computed by taking the difference between the κ-map data and scaled Σ-map (ICM gas) data. This corresponds to the amount of dark matter (not a falsifiable prediction) necessary to explain the Bullet Cluster 1E0657-558 data using Einstein/Newton gravity theory.

2 THE THEORY

2.1 Modified gravity

Analysis of the recent X-ray data from the Bullet Cluster 1E0657-558 (Markevitch 2006), probed by our computation in MOG, provides direct evidence that the convergence κ-map reconstructed from strong and weak gravitational lensing observations (Clowe et al. 2006a; Bradač et al. 2006; Clowe et al. 2006b) correctly accounts for all of the baryons in each of the main and subclusters including all of the galaxies in the regions near the main CD and the subcluster's BCG. The available baryonic mass, in addition to a second-rank skew symmetric tensor field (in MSTG), or massive vector field (in STVG), are the only properties of the system which contribute to the running gravitational coupling, $G(r)$. It is precisely this effect which allows MOG to fulfil its requirement as a relativistic theory of gravitation to correctly describe astrophysical phenomena without the necessity of dark matter (Moffat 2005, 2006a,b). MOG contains a running gravitational coupling – in the infrared (IR) at astrophysical scales – which has successfully been applied to galaxy rotation curves (Brownstein & Moffat 2006a), X-ray cluster masses (Brownstein & Moffat 2006b), and is within limits set by Solar system observations (Brownstein & Moffat 2006c).

The weak field, point particle spherically symmetric acceleration law in MOG is obtained from the action principle for the relativistic equations of motion of a test particle in Moffat (2005, 2006a). The weak field point particle gravitational potential for a static spherically symmetric system consists of two parts:

$$\Phi(r) = \Phi_N(r) + \Phi_Y(r), \tag{1}$$

where

$$\Phi_N(r) = -\frac{G_\infty M}{r} \tag{2}$$

and

$$\Phi_Y(r) = \sigma\frac{\exp(-\mu r)}{r} \tag{3}$$

denote the Newtonian and Yukawa potentials, respectively. M denotes the total constant mass of the system and μ denotes the effective mass of the vector particle in STVG. The Poisson equations for $\Phi_N(\boldsymbol{r})$ and $\Phi_Y(\boldsymbol{r})$ are given by

$$\nabla^2\Phi_N(\boldsymbol{r}) = -G_\infty\rho(\boldsymbol{r}) \tag{4}$$

and

$$(\nabla^2 - \mu^2)\Phi_Y(\boldsymbol{r}) = \frac{\sigma}{M}\rho(\boldsymbol{r}), \tag{5}$$

respectively. For sufficiently weak fields, we can assume that the Poisson equations (4) and (5) are uncoupled and determine the potentials $\Phi_N(\boldsymbol{r})$ and $\Phi_Y(\boldsymbol{r})$ for non-spherically symmetric systems, which can be solved analytically and numerically. The Green's function for the Yukawa Poisson equation is given by

$$(\nabla^2 - \mu^2)\Delta_Y(\boldsymbol{r}) = -\delta^3(\boldsymbol{r}). \tag{6}$$

The full solutions to the potentials are given by

$$\Phi_N(\boldsymbol{r}) = -G_\infty\int \mathrm{d}^3\boldsymbol{r}'\frac{\rho(\boldsymbol{r}')}{|\boldsymbol{r}-\boldsymbol{r}'|} \tag{7}$$

and

$$\Phi_Y(\boldsymbol{r}) = \frac{\sigma}{\int \mathrm{d}^3\boldsymbol{r}'\rho(\boldsymbol{r}')}\int \mathrm{d}^3\boldsymbol{r}'\frac{\exp(-\mu|\boldsymbol{r}-\boldsymbol{r}'|)\rho(\boldsymbol{r}')}{|\boldsymbol{r}-\boldsymbol{r}'|}. \tag{8}$$

For a delta function source density

$$\rho(\boldsymbol{r}) = M\delta^3(\boldsymbol{r}), \tag{9}$$

we obtain the point particle solutions of equations (2) and (3).

The modified acceleration law is obtained from

$$\boldsymbol{a}(\boldsymbol{r}) = -\nabla\Phi = -[\nabla\Phi_N(\boldsymbol{r}) + \nabla\Phi_Y(\boldsymbol{r})]. \tag{10}$$

Let us set

$$G_\infty = G_\mathrm{N}\left[1 + \left(\frac{M_0}{\int \mathrm{d}^3\boldsymbol{r}'\rho(\boldsymbol{r}')}\right)^{1/2}\right], \tag{11}$$

$$\sigma = G_\mathrm{N}[M_0\int \mathrm{d}^3\boldsymbol{r}'\rho(\boldsymbol{r}')]^{1/2}, \tag{12}$$

where M_0 is a constant and G_N denotes Newton's gravitational constant. From equations (7), (8) and (10), we obtain

$$\begin{aligned}\boldsymbol{a}(\boldsymbol{r}) = -G_\mathrm{N}&\int \mathrm{d}^3\boldsymbol{r}'\frac{(\boldsymbol{r}-\boldsymbol{r}')\rho(\boldsymbol{r}')}{|\boldsymbol{r}-\boldsymbol{r}'|^3}\\ &\times\left\{1 + \left(\frac{M_0}{\int \mathrm{d}^3\boldsymbol{r}'\rho(\boldsymbol{r}')}\right)^{1/2}\right.\\ &\left.\times[1 - \exp(-\mu|\boldsymbol{r}-\boldsymbol{r}'|)(1+\mu|\boldsymbol{r}-\boldsymbol{r}'|)]\right\}.\end{aligned} \tag{13}$$

We can write this equation in the form:

$$\boldsymbol{a}(\boldsymbol{r}) = -\int \mathrm{d}^3\boldsymbol{r}'\frac{(\boldsymbol{r}-\boldsymbol{r}')\rho(\boldsymbol{r}')}{|\boldsymbol{r}-\boldsymbol{r}'|^3}G(\boldsymbol{r}-\boldsymbol{r}'), \tag{14}$$

where

$$\begin{aligned}G(\boldsymbol{r}-\boldsymbol{r}') = G_\mathrm{N}&\left\{1 + \left(\frac{M_0}{\int \mathrm{d}^3\boldsymbol{r}'\rho(\boldsymbol{r}')}\right)^{1/2}\right.\\ &\left.\times[1 - \exp(-\mu|\boldsymbol{r}-\boldsymbol{r}'|)(1+\mu|\boldsymbol{r}-\boldsymbol{r}'|)]\right\}.\end{aligned} \tag{15}$$

For a static spherically symmetric point particle system, we obtain using equation (9) the effective modified acceleration law:

$$a(r) = -\frac{G(r)M(r)}{r^2}, \tag{16}$$

where

$$G(r) = G_\mathrm{N}\left\{1 + \sqrt{\frac{M_0}{M}}\left[1 - \exp(-r/r_0)\left(1 + \frac{r}{r_0}\right)\right]\right\}. \tag{17}$$

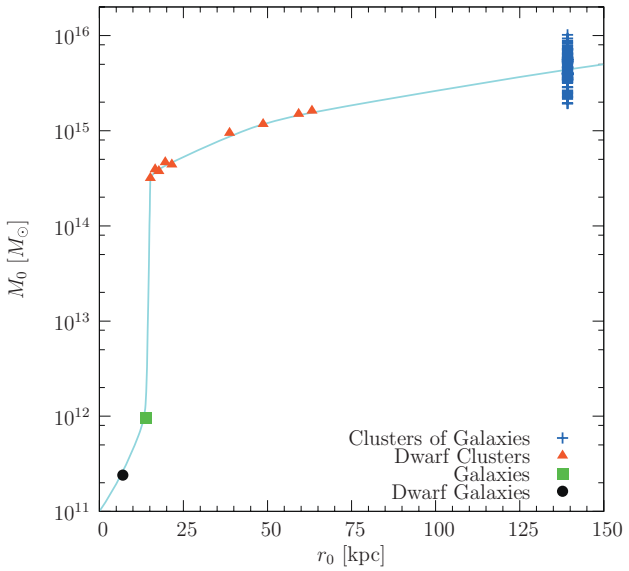

Figure 2. Running scales in MOG. A plot of the MOG mass scale, M_0, versus the MOG range parameter, r_0, compiled from published fits to galaxy rotation curves and X-ray cluster masses (Brownstein & Moffat 2006a,b). The values of M_0 versus r_0 are plotted for galaxies with green squares, dwarf galaxies with black circles, clusters of galaxies with blue crosses and dwarf clusters of galaxies with red triangles.

Here, M is the total baryonic mass of the system and we have set $\mu = 1/r_0$ and r_0 is a distance range parameter. We observe that $G(r) \to \mathrm{G_N}$ as $r \to 0$.

For the spherically symmetric static solution in MOG, the modified acceleration law equation (16) is determined by the baryon density and the parameters G_N, M_0 and r_0. However, the parameters M_0 and r_0 are scaling parameters that vary with distance, r, according to the field equations for the scalar fields $\omega(r) \propto M_0(r)$ and $\mu(r) = 1/r_0(r)$, obtained from the action principle (Moffat 2006a). In principle, solutions of the effective field equations for the variations of $\omega(r)$ and $\mu(r)$ can be derived given the potentials $V(\omega)$ and $V(\mu)$ in equations (24) and (26) of Moffat (2006a). However, at present the variations of $\omega(r)$ and $\mu(r)$ are empirically determined from the galaxy rotation curve and X-ray cluster mass data (Brownstein & Moffat 2006a,b).

In Fig. 2, we display the values of M_0 and r_0 for spherically symmetric systems obtained from the published fits to the galaxy rotation curves for dwarf galaxies, elliptical galaxies and spiral galaxies, and the fits to (normal and dwarf) X-ray cluster masses. A complete continuous relation between M_0 and r_0 at all mass scales needs to be determined from the MOG that fits the empirical mass scales and distance scales shown in Fig. 2. This will be a subject of future investigations.

The modifications to gravity leading to equation (17) would be negated by the vanishing of either $M_0 \to 0$ or the $r_0 \to \infty$ IR limit. These scale parameters are not to be taken as universal constants, but are source-dependent and scale according to the system. This is precisely the opposite case in MOND, where the Milgrom acceleration, $a_{0\mathrm{Milgrom}} = 1.2 \times 10^{-8}\,\mathrm{cm\ s^{-2}}$ (Milgrom 1983), is a phenomenologically derived universal constant – arising from a classical modification to the Newtonian potential. Additionally, MOND has an arbitrary function, $\mu(x)$, which should be counted among the degrees of freedom of that theory. Conversely, MOG does not arise from a classical modification but from the equations of motion of a relativistic modification to general relativity.

The cases we have examined until now have been modelled assuming spherical symmetry. These include 101 galaxy rotation curves (Brownstein & Moffat 2006a), 106 X-ray cluster masses (Brownstein & Moffat 2006b) and the gravitational solution to the Pioneer 10/11 anomaly in the Solar system (Brownstein & Moffat 2006c). In applications of MOG, we vary the gravitational coupling G, the vector field ϕ_μ coupling to matter and the effective mass μ of the vector field according to a renormalization group (RG) flow description of quantum gravity theory formulated in terms of an effective classical action (Moffat 2005, 2006a). Large IR renormalization effects may cause the effective coupling constants to run with momentum. A cut-off leads to spatially varying values of G, M_0 and r_0 and these values increase in size according to the mass scale and distance scale of a physical system (Reuter & Weyer 2006).

The spatially varying dimensionless gravitational coupling is given by

$$\mathcal{G}(r) \equiv \frac{G(r)}{G_\mathrm{N}} = 1 + \sqrt{\frac{M_0}{M(r)}}\left\{1 - \exp\left(-\frac{r}{r_0}\right)\left(1 + \frac{r}{r_0}\right)\right\}, \tag{18}$$

where

(i) $G_\mathrm{N} = 6.6742 \times 10^{-11}\,\mathrm{m^3\,kg\ s^{-2}}$ is the ordinary (terrestrial) Newtonian gravitational constant measured experimentally,[2]

(ii) $M(r)$ is the total (ordinary) mass enclosed in a sphere or radius, r. This may include all of the visible (X-ray) ICM gas and all of the galactic (baryonic) matter, but none of the non-baryonic dark matter.

(iii) M_0 is the MOG mass scale (usually measured in units of [$\mathrm{M_\odot}$]),

(iv) r_0 is the MOG range parameter (usually measured in units of [kpc]).

The dimensionless gravitational coupling, $\mathcal{G}(r)$, of equation (18), approaches an asymptotic value as $r \to \infty$:

$$\mathcal{G}_\infty = 1 + \sqrt{\frac{M_0}{M}}, \tag{19}$$

where M is the total baryonic mass of the system. Conversely, taken in the limit of $r \ll r_0$, $G(r) \to \mathrm{G_N}$ or $\mathcal{G}(r) \to 1$ down to the Planck length.

In order to apply the MOG model of equation (18) to the Bullet Cluster 1E0657-558, we must first generalize the spherically symmetric case. Our approach follows a sequence of approximations:

(i) Treat the subcluster as a perturbation, and neglect it as a zeroth-order approximation.

(ii) Treat the subcluster as a perturbation, and shift the origin of the gravitational coupling, $\mathcal{G}(r)$, towards the subcluster (towards the centre-of-mass of the system).

(iii) Use the concentric cylinder mass $M(R)$ as an approximation for $M(r)$, and shift that towards the subcluster (towards the MOG centre).

(iv) Treat the subcluster as a perturbation, and utilize the isothermal sphere model to approximate $M(R)$ and shift that towards the subcluster [towards the centre-of-mass of the system – where the origin of $\mathcal{G}(r)$ is located].

2.2 The King β-model for the Σ-map

Starting with the zeroth-order approximation, we neglect the subcluster, and perform a best fit to determine a spherically symmetric

[2] NIST 2002 CODATA value.

King β-model density of the main cluster. We assume the main cluster gas (neglecting the subcluster) is in nearly hydrostatic equilibrium with the gravitational potential of the galaxy cluster. Within a few core radii, the distribution of gas within a galaxy cluster may be fit by a King 'β-model'. The observed surface brightness of the X-ray cluster can be fit to a radial distribution profile (Chandrasekhar 1960; King 1966):

$$I(r) = I_0 \left[1 + \left(\frac{r}{r_c}\right)^2\right]^{-3\beta+1/2}, \tag{20}$$

resulting in best-fitting parameters, β and r_c. A deprojection of the β-model of equation (20) assuming a nearly isothermal gas sphere then results in a physical gas density distribution (Cavaliere & Fusco-Femiano 1976):

$$\rho(r) = \rho_0 \left[1 + \left(\frac{r}{r_c}\right)^2\right]^{-3\beta/2}, \tag{21}$$

where $\rho(r)$ is the ICM mass density profile and ρ_0 denotes the central density. The mass profile associated with this density is given by

$$M(r) = 4\pi \int_0^r \rho(r') r'^2 dr', \tag{22}$$

where $M(r)$ is the total mass contained within a sphere of radius r. Galaxy clusters are observed to have finite spatial extent. This allows an approximate determination of the total mass of the galaxy cluster by first solving equation (21) for the position, $r_{\rm out}$, at which the density, $\rho(r_{\rm out})$, drops to $\approx 10^{-28}$ g cm^{-3}, or 250 times the mean cosmological density of baryons:

$$r_{\rm out} = r_c \left[\left(\frac{\rho_0}{10^{-28}\ {\rm g\ cm^{-3}}}\right)^{2/3\beta} - 1\right]^{1/2}. \tag{23}$$

Then, the total mass of the ICM gas may be taken as $M_{\rm gas} \approx M(r_{\rm out})$:

$$M_{\rm gas} = 4\pi \int_0^{r_{\rm out}} \rho_0 \left[1 + \left(\frac{r'}{r_c}\right)^2\right]^{-3\beta/2} r'^2\, {\rm d}r'. \tag{24}$$

To make contact with the experimental data, we must calculate the surface mass density by integrating $\rho(r)$ of equation (21) along the line-of-sight:

$$\Sigma(x, y) = \int_{-z_{\rm out}}^{z_{\rm out}} \rho(x, y, z)\, {\rm d}z, \tag{25}$$

where

$$z_{\rm out} = \sqrt{r_{\rm out}^2 - x^2 - y^2}. \tag{26}$$

Substituting equation (21) into equation (25), we obtain

$$\Sigma(x, y) = \rho_0 \int_{-z_{\rm out}}^{z_{\rm out}} \left[1 + \frac{x^2 + y^2 + z^2}{r_c^2}\right]^{-3\beta/2} {\rm d}z. \tag{27}$$

This integral becomes tractable by making a substitution of variables:

$$u^2 = 1 + \frac{x^2 + y^2}{r_c^2}, \tag{28}$$

so that

$$\begin{aligned}\Sigma(x, y) &= \rho_0 \int_{-z_{\rm out}}^{z_{\rm out}} \left[u^2 + \left(\frac{z}{r_c}\right)^2\right]^{-3\beta/2} {\rm d}z \\ &= \frac{\rho_0}{u^{3\beta}} \int_{-z_{\rm out}}^{z_{\rm out}} \left[1 + \left(\frac{z}{u r_c}\right)^2\right]^{-3\beta/2} {\rm d}z \\ &= 2\frac{\rho_0}{u^{3\beta}} z_{\rm out} F\left(\left[\frac{1}{2}, \frac{3}{2}\beta\right], \left[\frac{3}{2}\right], -\left(\frac{z_{\rm out}}{u r_c}\right)^2\right),\end{aligned} \tag{29}$$

where we have made use of the hypergeometric function, $F([a, b], [c], z)$. Substituting equation (28) into equation (29) gives

$$\begin{aligned}\Sigma(x, y) = 2\rho_0 z_{\rm out} &\left(1 + \frac{x^2 + y^2}{r_c^2}\right)^{-3\beta/2} \\ &\times F\left(\left[\frac{1}{2}, \frac{3}{2}\beta\right], \left[\frac{3}{2}\right], -\frac{z_{\rm out}^2}{x^2 + y^2 + r_c^2}\right).\end{aligned} \tag{30}$$

We next define

$$\Sigma_0 \equiv \Sigma(0, 0) = 2\rho_0 z_{\rm out} F\left(\left[\frac{1}{2}, \frac{3}{2}\beta\right], \left[\frac{3}{2}\right], -\left(\frac{z_{\rm out}}{r_c}\right)^2\right), \tag{31}$$

which we substitute into equation (30), yielding

$$\begin{aligned}\Sigma(x, y) = \Sigma_0 &\left(1 + \frac{x^2 + y^2}{r_c^2}\right)^{-3\beta/2} \\ &\times \frac{F\left(\left[\frac{1}{2}, \frac{3}{2}\beta\right], \left[\frac{3}{2}\right], -\frac{z_{\rm out}^2}{x^2+y^2+r_c^2}\right)}{F\left(\left[\frac{1}{2}, \frac{3}{2}\beta\right], \left[\frac{3}{2}\right], -\frac{z_{\rm out}^2}{r_c^2}\right)}.\end{aligned} \tag{32}$$

In the limit $z_{\rm out} \gg r_c$, the hypergeometric functions simplify to Γ functions, and equations (31) and (32) result in the simple, approximate solutions:

$$\Sigma_0 = \sqrt{\pi}\rho_0 r_c \frac{\Gamma\left(\frac{3\beta-1}{2}\right)}{\Gamma\left(\frac{3}{2}\beta\right)} \tag{33}$$

and

$$\Sigma(x, y) = \Sigma_0 \left(1 + \frac{x^2 + y^2}{r_c^2}\right)^{-(3\beta-1)/2}, \tag{34}$$

which we may, in principle, fit to the Σ-map data to determine the King β-model parameters, β, r_c and ρ_0.

2.3 Deriving the weighted surface mass density from the convergence κ-map

The goal of the strong and weak lensing survey of Clowe et al. (2006a), Bradač et al. (2006) and Clowe et al. (2006b) was to obtain a convergence κ-map by measuring the distortion of images of background galaxies (sources) caused by the deflection of light as it passes the Bullet Cluster 1E0657-558 (lens). The distortions in image ellipticity are only measurable statistically with large numbers of sources. The data were first corrected for smearing by the point spread function in the image, resulting in a noisy, but direct, measurement of the reduced shear $g = \gamma/(1 - \kappa)$. The shear, γ, is the anisotropic stretching of the galaxy image, and the convergence, κ, is the shape-independent change in the size of the image. By recovering the κ-map from the measured reduced shear field, a measure of the local curvature is obtained. In Einstein's general relativity, the local curvature is related to the distribution of mass/energy, as it is in MOG. In Newtonian gravity theory, the relationship between the κ-map and the surface mass density becomes very simple, allowing one to refer to κ as the scaled surface mass density [see e.g. chapter 4 of Peacock (2003) for a derivation]:

$$\kappa(x, y) = \int \frac{4\pi G_{\rm N}}{c^2} \frac{D_{\rm l} D_{\rm ls}}{D_{\rm s}} \rho(x, y, z) {\rm d}z \equiv \frac{\Sigma}{\Sigma_{\rm c}}, \tag{35}$$

where

$$\Sigma(x, y) = \int \rho(x, y, z)\, {\rm d}z, \tag{36}$$

is the surface mass density and

$$\Sigma_c = \frac{c^2}{4\pi G_N}\frac{D_s}{D_l D_{ls}} \approx 3.1 \times 10^9\ \mathrm{M}_\odot\ \mathrm{kpc}^{-2} \tag{37}$$

is the Newtonian critical surface mass density (with vanishing shear), D_s is the angular distance to a source (background) galaxy, D_l is the angular distance to the lens (Bullet Cluster 1E0657-558) and D_{ls} is the angular distance from the Bullet Cluster 1E0657-558 to a source galaxy. The result of equation (37) is equivalent to

$$\frac{D_l D_{ls}}{D_s} \approx 540\ \mathrm{kpc}. \tag{38}$$

Since there is a multitude of source galaxies, these distances become 'effective', as is the numeric value presented in equation (37), quoted from Clowe, Gonzalez & Markevitch (2004) without estimate of the uncertainty. In fact, due to the multitude of sources in the lensing survey, both D_s and D_{ls} are distributions in (x, y). However, it is a common practice to move them outside the integral, as a necessary approximation.

We may obtain a similar result in MOG, as was shown in Moffat (2006b), by promoting the Newtonian gravitational constant, G_N to the running gravitational coupling, $G(r)$, but approximating $G(r)$ as sufficiently slow varying to allow it to be removed from the integral. We have in general,

$$\kappa(x, y) = \int \frac{4\pi G(r)}{c^2}\frac{D_l D_{ls}}{D_s}\rho(x, y, z)\,\mathrm{d}z \equiv \frac{\Sigma(x, y)}{\Sigma_c(r)}, \tag{39}$$

and we assume that

$$\Sigma_c(r) = \frac{c^2}{4\pi G(r)}\frac{D_s}{D_l D_{ls}} = \frac{G_N}{G(r)}\Sigma_c = \frac{\Sigma_c}{\mathcal{G}(r)}, \tag{40}$$

where we applied equation (18). However, equations (39) and (40) are only valid in the thin lens approximation. For the Bullet Cluster 1E0657-558, the thin lens approximation is inappropriate, and we must use the correct relationship between κ and Σ:

$$\kappa(x, y) = \int \frac{4\pi G(r)}{c^2}\frac{D_l D_{ls}}{D_s}\rho(x, y, z)\,\mathrm{d}z \equiv \frac{\bar{\Sigma}(x, y)}{\Sigma_c}, \tag{41}$$

where

$$\bar{\Sigma}(x, y) = \int \mathcal{G}(r)\rho(x, y, z)\,\mathrm{d}z \tag{42}$$

is the weighted surface mass density [weighted by the dimensionless gravitational coupling $\mathcal{G}(r)$ of equation 18] and Σ_c is the usual Newtonian critical surface mass density equation (37).

For the remainder of this paper, we will use equations (18), (37), (41) and (42) to reconcile the experimental observations of the gravitational lensing κ-map with the X-ray imaging Σ-map. We can already see from these equations that how in MOG the convergence, κ, is now related to the weighted surface mass density, $\bar{\Sigma}$, so

"... κ is no longer a measurement of the surface density, but is a non-local function whose overall level is still tied to the amount of mass. For complicated system geometries, such as a merging cluster, the multiple peaks can deflect, suppress or enhance some of the peaks (Clowe et al. 2006b)."

3 THE SURFACE DENSITY MAP FROM X-RAY IMAGE OBSERVATIONS

3.1 The Σ-map

With an advance of the 2006 November 15 data release (Clowe et al. 2006c), we began a precision analysis to model the gross features of the surface density Σ-map data in order to gain insight into the 3D matter distribution, $\rho(r)$, and to separate the components into a model representing the main cluster and the subcluster – the remainder after subtraction.

The Σ-map is shown in false colour in Fig. 3. There are two distinct peaks in the surface density Σ-map – the primary peak centred at the main cluster and the secondary peak centred at the subcluster. The main cluster gas is the brightly glowing (yellow) region to the left-hand side of the subcluster gas, which is the nearly equally bright shockwave region (arrowhead shape to the right-hand side). The κ-map observed peaks, the CD galaxy of the main cluster, the brightest cluster galaxy (BCG) of the subcluster and the MOG predicted gravitational centre are shown in Fig. 3 for comparison. J2000 and map (x, y) coordinates are listed in Table 1.

We may now proceed to calculate the best-fitting parameters, β, r_c and ρ_0, of the King β-model of equations (33) and (34) by applying a non-linear least-squares fitting routine (including estimated errors) to the entire Σ-map, or alternatively by performing the fit to a subset of the Σ-map on a straight line connecting the main cluster Σ-map peak ($R \equiv 0$) to the main CD, and then extrapolating the fit to the entire map. This reduces the complexity of the calculation to a simple algorithm, but is not guaranteed to yield a global best fit. However, our approximate best fit will prove to agree with the Σ-map everywhere, except at the subcluster (which is neglected for the best fit).

The scaled surface density Σ-map data are shown in solid red in Fig. 4. The unmodelled peak (at $R \sim 300$ kpc) is due to the subcluster. The best fit to the King β-model of equation (34) is shown in Fig. 4 in short-dashed blue, and corresponds to

$$\beta = 0.803 \pm 0.013, \tag{43}$$

$$r_c = 278.0 \pm 6.8\ \mathrm{kpc}, \tag{44}$$

where the value of the Σ-map at the main cluster peak is constrained to the observed value,

$$\Sigma_0 = 1.6859 \times 10^{10}\frac{\mathrm{M}_\odot}{\mathrm{pixel}^2}\left(\frac{1\ \mathrm{pixel}}{8.528\ \mathrm{kpc}}\right)^2 = 2.3181 \times 10^8\ \mathrm{M}_\odot\ \mathrm{kpc}^{-2}. \tag{45}$$

We may now solve equation (33) for the central density of the main cluster,

$$\rho_0 = \frac{\Sigma_0}{\sqrt{\pi} r_c}\frac{\Gamma\left(\frac{3}{2}\beta\right)}{\Gamma\left(\frac{3\beta-1}{2}\right)} = 3.34 \times 10^5\ \mathrm{M}_\odot\ \mathrm{kpc}^{-2}. \tag{46}$$

The values of the parameters β, r_c and ρ_0 completely determine the King β-model for the density, $\rho(r)$, of equation (21) of the main cluster X-ray gas. We provide a comparison of the full Σ-map data (Fig. 5, in red) with the result of the surface density Σ-map derived from the best-fitting King β-model to the main cluster (Fig. 5, in blue).

Substituting equations (43), (44) and (46) into equation (23), we obtain the main cluster outer radial extent,

$$r_{out} = 2620\ \mathrm{kpc}, \tag{47}$$

the distance at which the density, $\rho(r_{out})$, drops to $\approx 10^{-28}\ \mathrm{g\,cm}^{-3}$, or 250 times the mean cosmological density of baryons. The total mass of the main cluster may be calculated by substituting equations (43), (44) and (46) into equation (24):

$$M_{gas} = 3.87 \times 10^{14}\ \mathrm{M}_\odot. \tag{48}$$

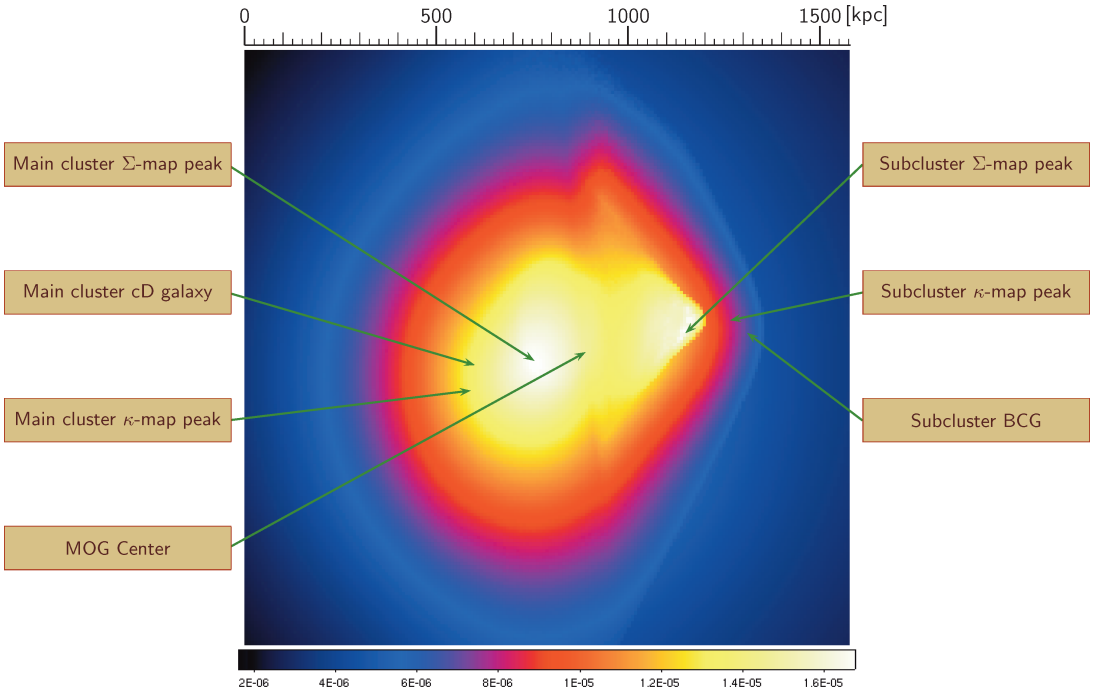

Figure 3. Surface density Σ-map. Data reconstructed from X-ray imaging observations of the Bullet Cluster 1E0657-558, 2006 November 15 data release (Clowe et al. 2006c). Σ-map observed peaks (local maxima) and κ-map observed peaks are shown for comparison. The CD galaxy of the main cluster, the BCG of the subcluster and the MOG predicted gravitational centre are shown. The colour-scale is shown at the bottom, in units of 10^{15} $M_\odot$ pixel^{-2}. The resolution of the Σ-map is 8.5 kpc pixel^{-1}, based on the measured redshift distance $\sim$ 260.0 kpc arcmin^{-1} of the Bullet Cluster 1E0657-558 (Bradač et al. 2006). The scale in kpc is shown at the top of the figure. J2000 and map (x,y) coordinates are listed in Table 1.

Table 1. The J2000 sky coordinates of the Bullet Cluster 1E0657-558, 2006 November 15 data release (Clowe et al. 2006c): main cluster and subcluster Σ-map and κ-map observed peaks, the CD galaxy of the main cluster, the BCG of the subcluster and the MOG predicted gravitational centre. The resolution of the Σ-map and κ-map is 8.5 and 15.4 kpc pixel^{-1}, respectively, based on the measured redshift distance $\sim$ 260.0 kpc arcmin^{-1} of the Bullet Cluster 1E0657-558 (Bradač et al. 2006).

Observation	J2000 coordinates		Σ-map	κ-map
	RA	Dec.	(x, y)	(x, y)
Main cluster Σ-map peak	$06^h{:}58^m{:}31\overset{s}{.}1$	$-55^\circ{:}56'{:}53\overset{''}{.}6$	(89, 89)	(340, 321)
Subcluster Σ-map peak	$06^h{:}58^m{:}20\overset{s}{.}4$	$-55^\circ{:}56'{:}35\overset{''}{.}9$	(135, 98)	(365, 326)
Main cluster κ-map peak	$06^h{:}58^m{:}35\overset{s}{.}6$	$-55^\circ{:}57'{:}10\overset{''}{.}8$	(70, 80)	(329, 317)
Subcluster κ-map peak	$06^h{:}58^m{:}17\overset{s}{.}0$	$-55^\circ{:}56'{:}27\overset{''}{.}6$	(149, 102)	(374, 327)
Main cluster CD	$06^h{:}58^m{:}35\overset{s}{.}3$	$-55^\circ{:}56'{:}56\overset{''}{.}3$	(71, 88)	(330, 320)
Subcluster BCG	$06^h{:}58^m{:}16\overset{s}{.}0$	$-55^\circ{:}56'{:}35\overset{''}{.}1$	(154, 98)	(375, 326)
MOG Centre	$06^h{:}58^m{:}27\overset{s}{.}6$	$-55^\circ{:}56'{:}49\overset{''}{.}4$	(105, 92)	(348, 322)

3.2 The gravitational coupling for the main cluster

As discussed in Section 2.1, in order to apply the MOG model of equation (18) to the Bullet Cluster 1E0657-558, we must first generalize the spherically symmetric case by treating the subcluster as a perturbation. In the zeroth-order approximation, we begin by neglecting the subcluster. According to the large (>100) galaxy cluster survey of Brownstein & Moffat (2006b), the MOG mass scale, M_0, is determined by a power law, depending only on the computed total cluster mass, $M_{\rm gas}$:

$$M_0 = (60.4 \pm 4.1) \times 10^{14}\ \mathrm{M}_\odot \left(\frac{M_{\rm gas}}{10^{14}\ \mathrm{M}_\odot} \right)^{0.39\pm0.10}. \qquad (49)$$

Substituting the result of equation (48) for the main cluster into equation (49), we obtain

$$M_0 = 1.02 \times 10^{16}\ \mathrm{M}_\odot, \qquad (50)$$

and substituting the result of equation (48) for M and equation (50) for the main cluster of Bullet Cluster 1E0657-558 into equation (19), we obtain

$$\mathcal{G}_\infty = 6.14. \qquad (51)$$

From Brownstein & Moffat (2006b), the MOG range parameter, r_0, depends only on the computed outer radial extent, $r_{\rm out}$:

$$r_0 = r_{\rm out}/10, \quad r_{\rm out} \leqslant 650\,\mathrm{kpc},$$
$$r_0 = 139.2\,\mathrm{kpc}, \quad r_{\rm out} > 650\,\mathrm{kpc}, \qquad (52)$$

from which we obtain

$$r_0 = 139.2\ \mathrm{kpc} \qquad (53)$$

for the main cluster.

The best-fitting King β-model parameters for the main cluster are listed in Table 2, and the MOG parameters for the main cluster are listed in Table 3. A plot of the dimensionless gravitational coupling

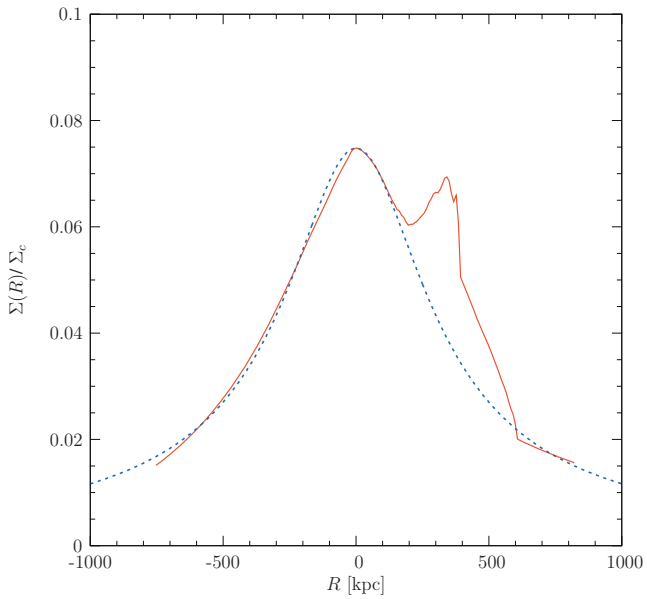

Figure 4. King β-model fit to scaled Σ-map. A cross-section of the scaled surface density Σ-map data reconstructed from X-ray imaging observations of the Bullet Cluster 1E0657-558, on a straight line connecting the main X-ray cluster peak ($R \equiv 0$ kpc) to the main CD galaxy ($R \approx -150$ kpc). The main cluster Σ-map data, taken from the 2006 November 15 data release (Clowe et al. 2006c), are shown in solid red, and the surface density Σ-map according to the best-fitting King β-model (neglecting the subcluster) of equation (34) is shown in short-dashed blue. The unmodelled peak (at $R \sim 300$ kpc) is due to the subcluster. We used the Clowe et al. (2004) value for the Newtonian critical surface mass density (with vanishing shear), $\Sigma_c = 3.1 \times 10^9\ \mathrm{M}_\odot\ \mathrm{kpc}^{-2}$. J2000 and map (x,y) coordinates are listed in Table 1. The best-fitting King β-model parameters are listed in Table 2.

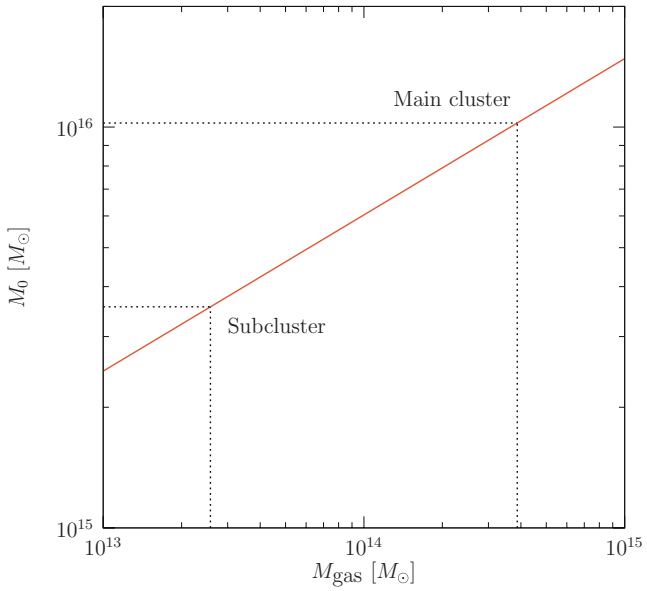

Figure 6. The MOG mass scale, M_0, versus $M_{\rm gas}$. A graphical calculation based on a power-law running of the MOG mass scale, M_0, depending on the total ICM gas mass, $M_{\rm gas}$, determined by the large (>100) galaxy cluster survey of Brownstein & Moffat (2006b). The computed values of $M_{\rm gas}$ and M_0 for the main and subcluster are listed in Table 3.

of equation (18) using the MOG parameter results of equations (50) and (53) for the main cluster (neglecting the subcluster) is plotted in Fig. 7 using a linear scale for the r-axis (left-hand side), and on a logarithmic scale for the r-axis (right-hand side).

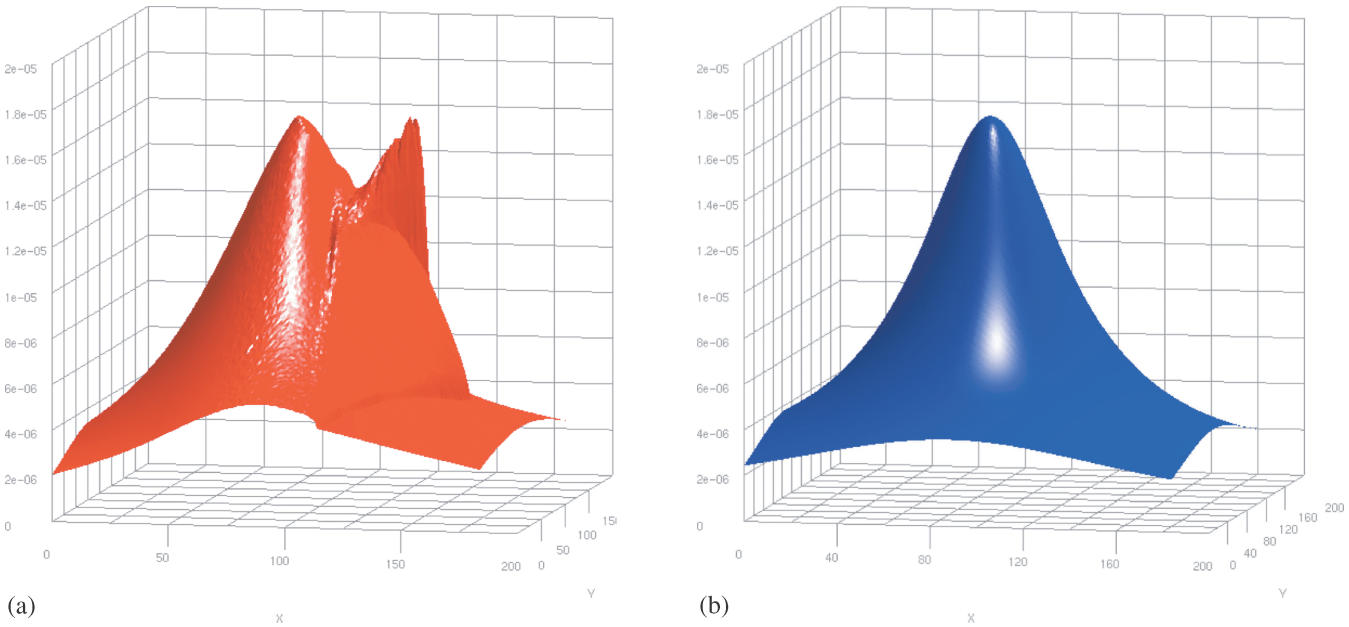

Figure 5. Comparison of the Σ-map data and the best-fitting King β-model. The surface density Σ-map data reconstructed from X-ray imaging observations of the Bullet Cluster 1E0657-558, 2006 November 15 data release (Clowe et al. 2006c) are shown in red (left-hand side). The surface density Σ-map according to the best-fitting King β-model (neglecting the subcluster) of equation (34) is shown in blue (right-hand side). The best-fitting King β-model parameters are listed in Table 2.

Table 2. The best-fitting King β-model parameters. Using a non-linear least-squares fitting routine, equations (33) and (34) are fit to the Σ-map data for the main cluster (neglecting the subcluster). Results of our calculation for the main and subcluster mass, $M_{\rm gas}$, and cluster outer radial extent, $r_{\rm out}$, are listed below. The best fit is shown in Figs 4 and 5 in blue, and may be compared to the data, in red.

King model	Main cluster	Subcluster
β	0.803 ± 0.013	...
$r_{\rm c}$	$278.0 \pm 6.8\,{\rm kpc}$	...
ρ_0	$3.34 \times 10^5\,{\rm M}_\odot\,{\rm kpc}^{-2}$	...
$M_{\rm gas}$	$3.87 \times 10^{14}\,{\rm M}_\odot$	$2.58 \times 10^{13}\,{\rm M}_\odot$
$r_{\rm out}$	2620 kpc	...

Table 3. MOG parameters. Results of calculation of the power-law running of the MOG mass scale, M_0, depending on the computed total cluster mass, $M_{\rm gas}$, according to the large (>100) galaxy cluster survey of Brownstein & Moffat (2006b) for the main and subcluster (shown graphically in Fig. 6), and the overall best fit to the κ-map; and the results for the MOG range parameter, r_0. Results of the calculations for the asymptotic value of the dimensionless gravitational coupling, $\mathcal{G}_\infty$, and the calculated X-ray temperature of the unperturbed isothermal sphere for the main cluster, T, are listed.

MOG	Main cluster	Subcluster	Best fit to κ-map
M_0	$1.02 \times 10^{16}\,{\rm M}_\odot$	$3.56 \times 10^{15}\,{\rm M}_\odot$	$3.07 \times 10^{15}\,{\rm M}_\odot$
r_0	139.2 kpc	...	208.8 kpc
$\mathcal{G}_\infty$	6.14	...	3.82
T	$15.5 \pm 3.9\,{\rm keV}$	...	...

3.3 The cylindrical mass profile

$\Sigma(x, y)$ is an integrated density along the line-of-sight, z, as shown in equation (36). By summing the Σ-map pixel-by-pixel, starting from the centre of the main cluster Σ-map peak, one is performing an integration of the surface density, yielding the mass,

$$M(R) = \int_0^R \Sigma(R') R'\,{\rm d}R', \tag{54}$$

enclosed by concentric cylinders of radius, $R = \sqrt{x^2 + y^2}$. We performed such a sum over the Σ-map data, and compared the result to the best-fitting King β-model derived in Section 3.1, with the parameters listed in Table 2. The results are shown in Fig. 8. The fact that the data and model are in good agreement provides evidence that the King β-model is valid in all directions from the main cluster Σ-map peak, and not just on the straight line connecting the peak to the main CD, where the fit was performed. The model deviates slightly from the data, underpredicting $M(R)$ for $R > 350$ kpc, which may be explained by the subcluster (which is included in the data, but not the model). The integrated mass profile arising from the dark matter analysis of the κ-map of equation (83) is shown for comparison on the same figure.

The ratio of dark matter to ICM gas for the main cluster is >3, which is significantly less than the average cosmological ratio of 5.68 discussed in Section 1.1, whereas one should expect the highest mass-to-light ratios from large, hot, luminous galaxy clusters, and the Bullet Cluster 1E0657-558 is certainly one of the largest and hottest.

3.4 The isothermal spherical mass profile

For a spherical system in hydrostatic equilibrium, the structure equation can be derived from the collisionless Boltzmann equation

$$\frac{\rm d}{{\rm d}r}\left[\rho(r)\sigma_{\rm r}^2\right] + \frac{2\rho(r)}{r}\left(\sigma_{\rm r}^2 - \sigma_{\theta,\phi}^2\right) = -\rho(r)\frac{{\rm d}\Phi(r)}{{\rm d}r}, \tag{55}$$

where $\Phi(r)$ is the gravitational potential for a point source, $\sigma_{\rm r}$ and $\sigma_{\theta,\phi}$ are mass-weighted velocity dispersions in the radial (r) and tangential (θ, ϕ) directions, respectively. For an isotropic system,

$$\sigma_{\rm r} = \sigma_{\theta,\phi}. \tag{56}$$

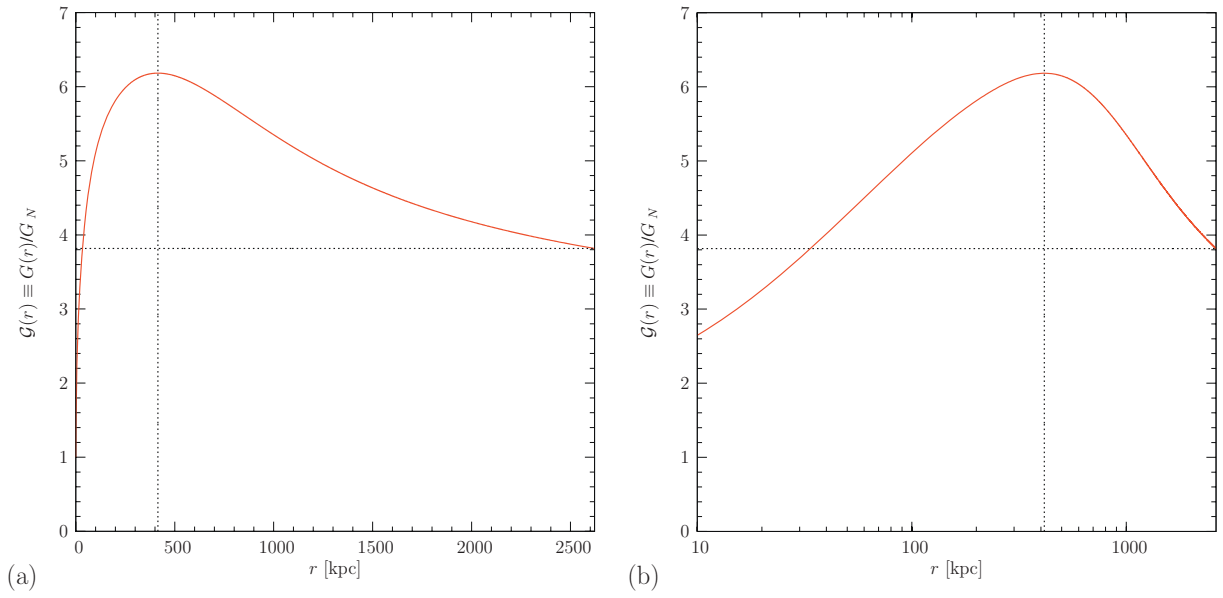

Figure 7. Plot of the dimensionless gravitational coupling, $\mathcal{G}(r) \equiv G(r)/G_{\rm N}$, of equation (18) versus the distance, r, in kpc. Shown in linear scale for the r-axis (left-hand side), and in logarithmic scale (right-hand side). J2000 and map (x, y) coordinates of the MOG centre ($R \equiv 0$ kpc) are listed in Table 1, and located with respect to the Σ-map and κ-map in Figs 3 and 12, respectively. The running gravitational coupling, $\mathcal{G}(r)$, shown here, corresponds to our best fit to the κ-map, listed in Table 3.

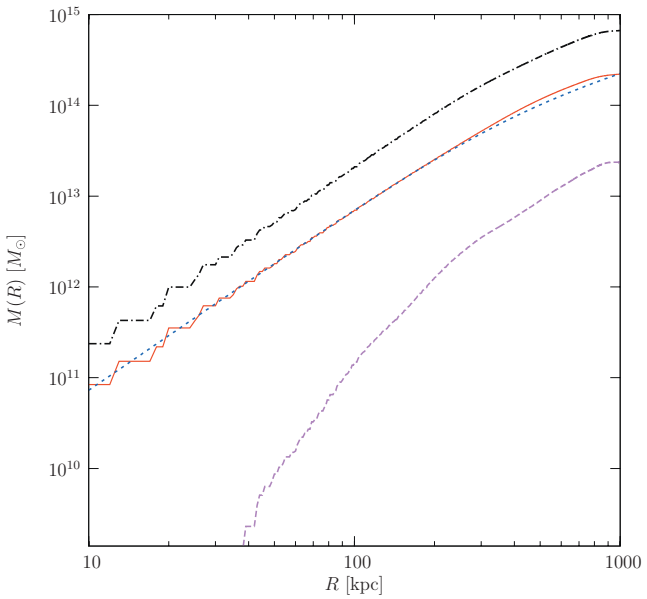

Figure 8. Cylindrical mass profile. The surface density Σ-map reconstructed from X-ray image observations of the Bullet Cluster 1E0657-558, 2006 November 15 data release (Clowe et al. 2006c) is integrated about the main cluster Σ-map peak ($R \equiv 0$), shown in solid red. The cylindrical mass profile derived from the best-fitting King β-model is shown in short-dashed blue, demonstrating a good agreement with the data. The long-dashed magenta line is the result of the galaxy subtraction of equations (78) and (79). The lack of galactic mass in the vicinity of the main cluster Σ-map peak at $R = 0$ is due to the merger. The dash–dotted black line is the result of the dark matter subtraction of equation (83). The dark matter dominates the ICM cluster gas by a factor of >3. J2000 and map (x, y) coordinates are listed in Table 1. The best-fitting King β-model parameters are listed in Table 2.

The pressure profile, $P(r)$, can be related to these quantities by

$$P(r) = \sigma_r^2 \rho(r). \tag{57}$$

Combining equations (55), (56) and (57), the result for the isotropic sphere is

$$\frac{dP(r)}{dr} = -\rho(r)\frac{d\Phi(r)}{dr}. \tag{58}$$

For a gas sphere with temperature profile, $T(r)$, the velocity dispersion becomes

$$\sigma_r^2 = \frac{kT(r)}{\mu_A m_p}, \tag{59}$$

where k is Boltzmann's constant, $\mu_A \approx 0.609$ is the mean atomic weight and m_p is the proton mass. We may now substitute equations (57) and (59) into equation (58) to obtain

$$\frac{d}{dr}\left[\frac{kT(r)}{\mu_A m_p}\rho(r)\right] = -\rho(r)\frac{d\Phi(r)}{dr}. \tag{60}$$

Performing the differentiation on the left-hand side of equation (58), we may solve for the gravitational acceleration:

$$\begin{aligned} a(r) &\equiv -\frac{d\Phi(r)}{dr} \\ &= \frac{kT(r)}{\mu_A m_p r}\left[\frac{d\ln(\rho(r))}{d\ln(r)} + \frac{d\ln(T(r))}{d\ln(r)}\right]. \end{aligned} \tag{61}$$

For the isothermal isotropic gas sphere, the temperature derivative on the right-hand side of equation (61) vanishes and the remaining derivative can be evaluated using the β-model of equation (21):

$$a(r) = -\frac{3\beta kT}{\mu_A m_p}\left(\frac{r}{r^2 + r_c^2}\right). \tag{62}$$

The dynamical mass in Newton's theory of gravitation can be obtained as a function of radial position by replacing the gravitational acceleration with Newton's law:

$$a_N(r) = -\frac{G_N M(r)}{r^2}, \tag{63}$$

so that equation (61) can be rewritten as

$$M_N(r) = -\frac{r}{G_N}\frac{kT}{\mu_A m_p}\left[\frac{d\ln(\rho(r))}{d\ln(r)} + \frac{d\ln(T(r))}{d\ln(r)}\right], \tag{64}$$

and the isothermal β-model result of equation (62) can be rewritten as

$$M_N(r) = \frac{3\beta kT}{\mu_A m_p G_N}\left(\frac{r^3}{r^2 + r_c^2}\right). \tag{65}$$

Similarly, the dynamical mass in MOG can be obtained as a function of radial position by substituting the MOG gravitational acceleration law (Moffat 2005, 2006a; Brownstein & Moffat 2006a,b)

$$a(r) = -\frac{G(r)M}{r^2}, \tag{66}$$

so that our result for the isothermal β-model becomes

$$M_{MOG}(r) = \frac{3\beta kT}{\mu_A m_p G(r)}\left(\frac{r^3}{r^2 + r_c^2}\right). \tag{67}$$

We can express this result as a scaled version of equation (64) or the isothermal case of equation (65):

$$\begin{aligned} M_{MOG}(r) &= \frac{M_N(r)}{\mathcal{G}(r)} \\ &= \left\{1 + \sqrt{\frac{M_0}{M_{MOG}(r)}} \right. \\ &\quad \left. \times \left[1 - \exp(-r/r_0)\left(1 + \frac{r}{r_0}\right)\right]\right\}^{-1} M_N(r), \end{aligned} \tag{68}$$

where we have substituted equation (18) for $\mathcal{G}(r)$. Equation (68) may be solved explicitly for $M_{MOG}(r)$ by squaring both sides and determining the positive root of the quadratic equation.

The scaling of the Newtonian dynamical mass by $\mathcal{G}(r)$ according to equation (68) answered the question of missing mass for the galaxy clusters of the >100 galaxy cluster survey of Brownstein & Moffat (2006b). The unperturbed Bullet Cluster 1E0657-558 is no exception! In Fig. 9, we plotted the MOG and the Newtonian dynamical masses, $M_{MOG}(r)$ and $M_N(r)$, respectively, and compared it to the spherically integrated best-fitting King β-model for the main cluster gas mass of equations (21) and (22) using the parameters listed in Table 2. The MOG temperature prediction due to the best fit is listed in Table 4 and is compared to experimental values.

As shown in Fig. 9, across the range of the r-axis, and throughout the radial extent of the Bullet Cluster 1E0657-558, the 1σ correlation between the gas mass, $M(r)$, and the MOG dynamical mass, $M_{MOG}(r)$, provides excellent agreement between theory and experiment. The same cannot be said of any theory of dark matter in which the X-ray surface density map is negligible in relation to the DM density. So, dark matter makes no prediction for the isothermal temperature, which has been measured to reasonable precision for many clusters, but simply 'accounts for missing mass'. Since there is no mysterious missing mass in MOG, the prediction should be taken seriously as direct confirmation of the theory, or at least as hard evidence for MOG.

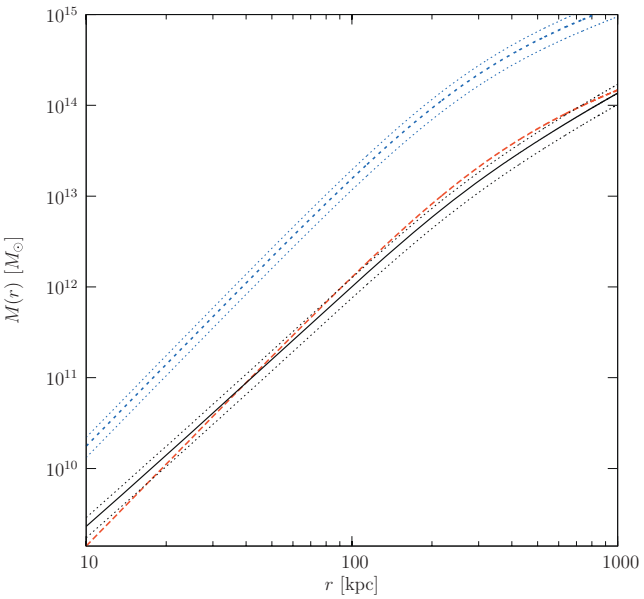

Figure 9. The spherically integrated mass profile of the main cluster ICM gas. The mass profile integrated King β-model, $M_{\rm gas}(r)$, from the Σ-map peak is shown in long-dashed red, derived from the surface density Σ-map data reconstructed from X-ray imaging observations of the Bullet Cluster 1E0657-558, 2006 November 15 data release (Clowe et al. 2006c). The surface density Σ-map according to the best-fitting King β-model (neglecting the subcluster) of equation (34) is shown in black (with uncertainty). The Newtonian dynamical mass (the dark matter paradigm) is shown in short-dashed blue. All masses are presented in units of $M_\odot$, and distances, r, in kpc. The strong correspondence between the data (red) and the MOG fit (black) across distance scales in the cluster from tens to thousands of kpc is significant. This is the first evidence that the X-ray imaging data for the cluster is behaving similar to the large (>100) galaxy cluster survey of Brownstein & Moffat (2006b). J2000 and map (x, y) coordinates are listed in Table 1. The best-fitting King β-model parameters are listed in Table 2. The best-fitting MOG parameters are listed in Table 3.

Table 4. The MOG best-fitting temperature is consistent with the experimental values for the main cluster isothermal temperature, the 1999 *ASCA+ROSAT* fit and the 1998 *ASCA* fit (Markevitch et al. 2002).

Year	Source – theory or experiment	T(keV)	Per cent error
2007	MOG Prediction	15.5 ± 3.9	
2002	Accepted experimental value	$14.8^{+1.7}_{-1.2}$	4.5
1999	*ASCA+ROSAT* fit	$14.5^{+2.0}_{1.7}$	6.5
1998	*ASCA* fit	17.4 ± 2.5	12.3

3.5 The subcluster subtraction

Provided the surface density Σ-map derived from the best-fitting King β-model of equation (34) is sufficiently close to the Σ-map data (consider Figs 4 and 5), the difference between the data and the β-model is the surface density Σ-map due to the subcluster. Our subcluster subtraction, shown in Figs 10 and 11, is based on a high-precision ($\chi^2 < 0.2$) best-fitting King β-model to the main cluster, which agrees with the main cluster surface mass Σ-map (data) within 1 per cent everywhere and to a mean uncertainty of 0.8 per cent. The subcluster subtraction is accurate down to $\rho = 10^{-28}\,{\rm g\,cm^{-3}} \sim 563.2\,{\rm M_\odot\,pc^{-3}}$ baryonic background density. After subtraction, the subcluster Σ-map peak takes a value of $1.30 \times 10^8\,{\rm M_\odot\,kpc^{-2}}$, whereas the full Σ-map has a value of $2.32 \times 10^8\,{\rm M_\odot\,kpc^{-2}}$ at the subcluster Σ-map peak. Thus, the subcluster (at its most dense position) provides only ≈ 56 per cent of the X-ray ICM, the rest is due to the extended distribution of the main cluster. The subcluster subtraction surface density Σ-map shown in Fig. 10 uses the same colour-scale as the full Σ-map shown in Fig. 3, for comparison. Fig. 11 is a stereogram of the subcluster-subtracted surface density Σ-map and the subcluster superposed on to the surface density Σ-map of the best-fitting King β-model to the main cluster. There is an odd X-ray bulge in Figs 10 and 11 which may be an artefact of the subtraction, or perhaps evidence of an as yet unidentified component.

Since the outer radial extent of the subcluster gas is less than 400 kpc, the Σ-map completely contains all of the subcluster gas mass. By summing the subcluster-subtracted Σ-map pixel-by-pixel over the entire Σ-map peak, one is performing an integration of the surface density, yielding the total subcluster mass. We performed such a sum over the subcluster-subtracted Σ-map data, obtaining

$$M_{\rm gas} = 2.58 \times 10^{13}\,{\rm M_\odot}, \tag{69}$$

for the mass of the subcluster gas, which is less than 6.7 per cent of the mass of main cluster gas (the best-fitting King β-model parameters are listed in Table 2.). This justifies our initial assumption that the subcluster may be treated as a perturbation in order to fit the main cluster to the King β-model. Our subsequent analysis of the thermal profile confirms that the main cluster X-ray temperature is nearly isothermal, lending further support to the validity of the King β-model.

We may now calculate the MOG mass scale, M_0, of the subcluster by substituting the subcluster gas mass, $M_{\rm gas}$, of equation (69) into the power-law relation of equation (49), yielding

$$M_0 = 3.56 \times 10^{15}\,{\rm M_\odot}, \tag{70}$$

as shown in Fig. 6. The computed values of $M_{\rm gas}$ and M_0 for the main and subcluster are listed in Table 3.

4 THE CONVERGENCE MAP FROM LENSING ANALYSIS

4.1 The κ-map

As tempting as it is to see the convergence κ-map of Fig. 12 – a false colour image of the strong and weak gravitational lensing reconstruction (Clowe et al. 2006a,b; Bradač et al. 2006) – as a photograph of the 'curvature' around the Bullet Cluster 1E0657-558, it is actually a reconstruction of all of the bending of light over the entire distance from the lensing event source towards the *HST*. The source of the κ-map is $\propto \int G_{\rm N}\rho(r)$, along the line-of-site, as in equation (35), $\propto G(r)\int \rho(r)$ as in equation (39), or $\propto \int G(r)\rho(r)$ as in equation (41). For the Bullet Cluster 1E0657-558, we are looking along a line-of-sight which is at least as long as indicated by a redshift of $z = 0.296$ (Gpc scale). The sources of the lensing events are in a large neighbourhood of redshifts, an estimated $z = 0.85 \pm 0.15$. This fantastic scale (several Gpc) is naturally far in excess of the distance scales involved in the X-ray imaging surface density Σ-map. It is an accumulated effect, but only over the range of the X-ray source – as much as 2.2 Mpc. A comparison of these two scales indicates that the distance scales within the Σ-map are 10^{-3} below the Gpc's scale of the κ-map.

Preliminary comments on the 2006 November 15 data release (Clowe et al. 2006c):

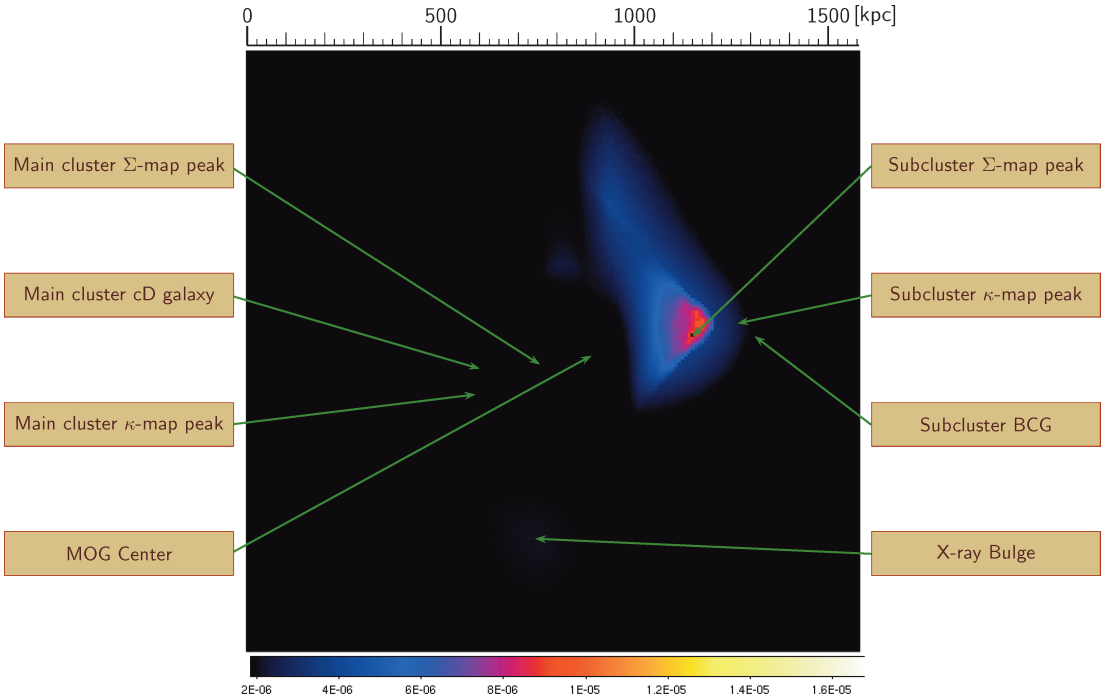

Figure 10. The subcluster-subtracted surface density Σ-map. Main cluster and subcluster κ-map observed peaks (local maxima) and Σ-map observed peaks are shown for comparison. The CD galaxy of the main cluster, the BCG of the subcluster and the MOG predicted gravitational centre are shown. The colour-scale is set to agree with Fig. 3 for comparison. J2000 and map (x, y) coordinates are listed in Table 1.

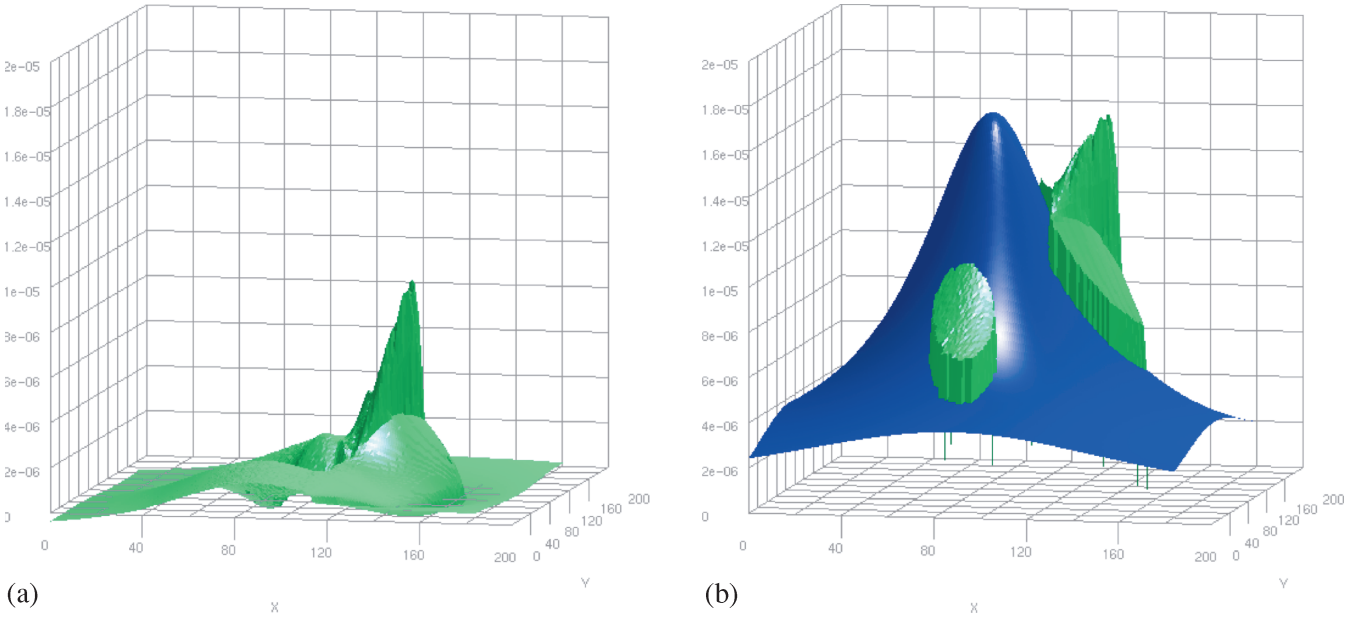

Figure 11. The subcluster-subtracted surface density Σ-map. (a) The result of the subcluster subtraction – the difference of the Σ-map data and our best-fitting King β-model of the main cluster. (b) The subcluster subtraction (green) superimposed on to the blue surface representing the Σ-map due to the best-fitting King β-model fit to main cluster (also shown in blue in Fig. 5). J2000 and map (x, y) coordinates are listed in Table 1. The best-fitting King β-model parameters are listed in Table 2.

(i) The conclusion of Clowe et al. (2006a) and Bradač et al. (2006), that the κ-map shows direct evidence for the existence of dark matter, may be premature. Until dark matter has been detected in the lab, it remains an open question whether a MOG theory, such as MOG, can account for the κ-map without non-baryonic dark matter. MOG, due to the varying gravitational coupling, equation (18), gives the Newtonian $1/r^2$ gravitational force law a considerable boost – 'extra gravity' as much as $\mathcal{G}_\infty \approx 6$ for the Bullet Cluster 1E0657-558.

(ii) It may be feasible that the mysterious plateau in the north-east corner of the κ-map is from some distribution of mass unrelated to the Bullet Cluster 1E0657-558. This 'background curvature'

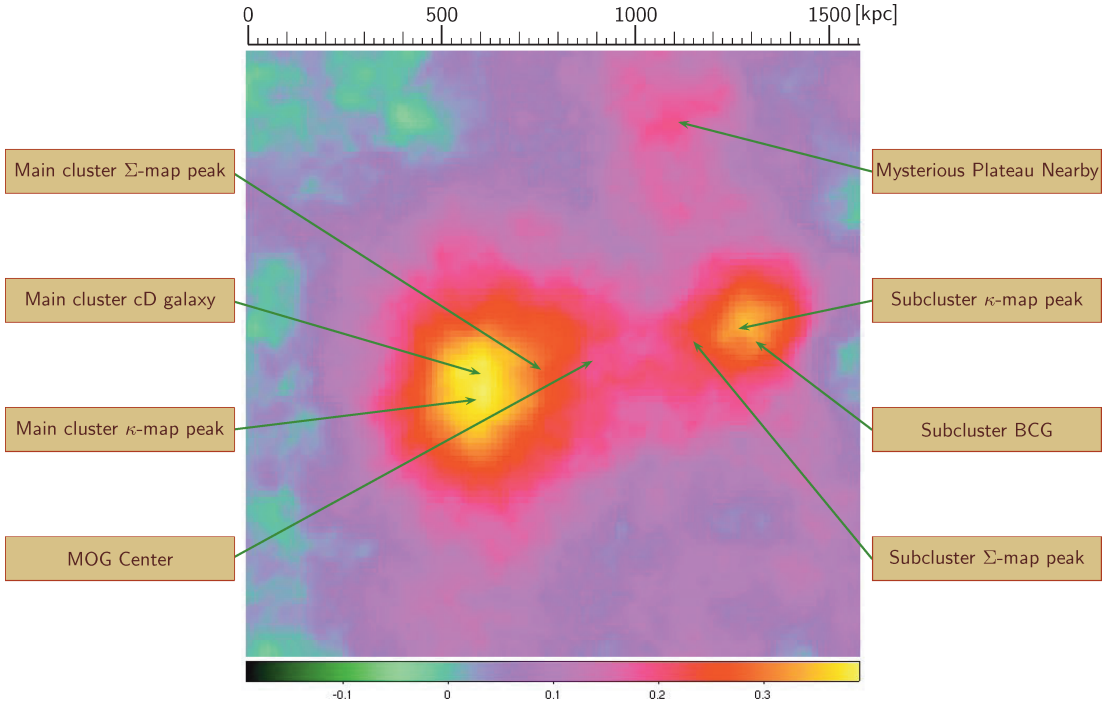

Figure 12. The surface density κ-map reconstructed from strong and weak gravitational lensing. Main cluster and subcluster of the Bullet Cluster 1E0657-558, 2006 November 15 data release κ-map (Clowe et al. 2006c) observed peaks (local maxima) and Σ-map observed peaks are shown for comparison. The CD galaxy of the main cluster, the BCG of the subcluster and the MOG predicted gravitational centre are shown. J2000 and map (x, y) coordinates are listed in Table 1.

contribution to the κ-map is one part of the uncertainty in the reconstruction. The second, dominant source of uncertainty must certainly be the estimate of the angular diameter distances between the source of the lensing event and the Bullet Cluster 1E0657-558, as shown in equation (37).

We have completed a large (>100) galaxy cluster survey in Brownstein & Moffat (2006b) that provides a statistically significant answer to the question of how much dark matter is expected. The relative abundance across the scales of the X-ray clusters would imply that the κ-map should peak at $\sim$1.0 as opposed to the 2006 November 15 data release (Clowe et al. 2006c), which peaks at a value of $\kappa \approx 0.38$ for the main cluster κ-map peak.
The dark matter paradigm cannot statistically account for such an observation without resorting to further ad hoc explanation, so the question of 'missing matter' may be irrelevant. The problem of 'extra gravity' due to MOG may be a step in the right direction, with our solution as the subject of the next section.

4.2 The MOG solution

The MOG κ-model we have developed in equations (41) and (42) can now be applied to the Bullet Cluster 1E0657-558. In order to model the κ-map, shown in Figs 12 and 14, in MOG, we must integrate the product of the dimensionless gravitational coupling $\mathcal{G}(r)$ of equation (18) with the mass density, $\rho(r)$, over the volume of the Bullet Cluster 1E0657-558. As discussed in Section 3.3, we may integrate the surface density Σ-map data according to equation (54) to obtain the integrated cluster gas mass about concentric cylinders centred about $R = 0$. However, what we require in the calculation of the $\mathcal{G}(r)$ of equation (18) is the integrated mass about concentric spheres,

$$M(r) = \int_0^{2\pi} \mathrm{d}\theta \int_0^{\pi} \sin\phi \, \mathrm{d}\phi \int_0^{r} r'^2 \, \mathrm{d}r' \rho(r', \theta, \phi). \tag{71}$$

The calculation of $M(r)$ using equation (71) is non-trivial, and we proceed by making a suitable approximation to the density, $\rho(r)$. As discussed in Section 2.1, we may apply a sequence of approximations to develop a MOG solution.

Zeroth-order approximation. We have obtained the spherically integrated best-fitting King β-model for the main cluster gas mass of equations (21) and (22) using the parameters listed in Table 2. By neglecting the subcluster, we have generated a base-line solution similar to every other spherically symmetric galaxy cluster. The result of substituting the spherically symmetric King β-model mass profile of equation (22) into equation (18) is shown in Fig. 7 for the dimensionless gravitational coupling, $\mathcal{G}(r)$. We obtain a zeroth-order, spherically symmetric approximation to the κ-map by substituting $\rho(r)$ and $\mathcal{G}(r)$ into equations (41) and (42) and integrating over the volume.

MOG centre. Treat the subcluster as a perturbation, and shift the origin of $\mathcal{G}(r)$ towards the subcluster (towards the centre-of-mass of the system). In this approximation, we continue to use the spherically integrated best-fitting King β-model for the main cluster gas mass of equations (21) and (22) using the parameters listed in Table 2, but we allow the subcluster to perturb (shift) the origin of $\mathcal{G}(r)$ towards the true centre-of-mass of the system. The integrals of equations (41) and (42) become non-trivial as the integrand is no longer spherically symmetric. We were able to obtain a full numerical integration, but the computation proved to be too time consuming ($\sim$70 000 numerical integrations to cover the

$185 \times 185\,\mathrm{pixel}^2$) to treat by means of a non-linear least-squares fitting routine.

Projective approximation. Approximate $M(r)$ with the concentric cylinder mass, $M(R)$ of equation (54), calculated directly from the Σ-map, where the pixel-by-pixel sum proceeds from the MOG centre. This is a poor approximation for small R (few pixels), but becomes very good for large R (many pixels), as can be seen by comparing Figs 8 and 9. The cylindrical mass, $M(R)$, can be computed directly from the Σ-map data using equation (54) without the need of a King β-model.

Isothermal β-model approximation. Treat the subcluster as a perturbation, and utilize the isothermal β-model of equation (68) to approximate $M(r)$ and shift that towards the subcluster (towards the MOG centre). This is a fully analytic expression, allowing ease of integration and an iterative fitting routine.

We will base our analysis on our best fit determined by the isothermal β-model approximation of equation (68), with $\mathcal{G}(r)$ located at the MOG centre, a distance away from the main cluster Σ-map peak towards the subcluster Σ-map peak. Since the dimensionless gravitational coupling, $\mathcal{G}(r)$, of equation (18) depends on $M(r)$, and the isothermal β-model of equation (68) depends on $\mathcal{G}(r)$, we must solve the system simultaneously. Let us rewrite equation (18) as

$$\mathcal{G}(r) = 1 + \sqrt{\frac{\xi(r)}{M(r)}}, \tag{72}$$

where

$$\xi(r) = M_0 \left\{ 1 - \exp\left(-\frac{r}{r_0} \right) \left(1 + \frac{r}{r_0} \right) \right\}^2. \tag{73}$$

We may solve equation (72) for

$$M(r) = \frac{\xi(r)}{(\mathcal{G}(r) - 1)^2}, \tag{74}$$

and equate this to the isothermal β-model of equation (68):

$$\frac{\xi(r)}{(\mathcal{G}(r) - 1)^2} = \frac{M_{\rm N}(r)}{\mathcal{G}(r)}, \tag{75}$$

and we may solve the quadratic equation for

$$\mathcal{G}(r) = 1 + \frac{\xi(r)}{2M_{\rm N}(r)} \left\{ 1 + \sqrt{\frac{4M_{\rm N}(r)}{\xi(r)} + 1} \right\}, \tag{76}$$

where $M_{\rm N}$ is the isothermal β-model Newtonian dynamic mass of equation (65). The result of equation (76) is a fully analytic function, as opposed to a hypergeometric integral, and may be easily computed across the full κ-map. There was a notable parameter degeneracy in choosing the MOG centre, the best fit corresponded to a distance of 140 kpc away from the main cluster Σ-map peak towards the subcluster Σ-map peak. This is reasonable since the Σ-map and κ-map data are 2D 'surface projections', due to the line-of-sight integral. The full simulation was run iteratively over a range of positions for the MOG centre, while covarying the MOG parameters, M_0 and r_0, the MOG mass scale and MOG range parameter, respectively. This yielded a best-fitting MOG model for the dimensionless gravitational coupling, $\mathcal{G}(r)$ of equation (18), where r is the distance from the MOG centre, as listed in Table 3. Our best fit to the κ-map corresponds to the MOG κ-model of equations (41) and (42). The best-fitting location of the MOG centre is provided on the Σ-map in Fig. 3, and the coordinates are listed in Table 1.

We show a 3D visualization of the convergence κ-map data in Fig. 14 (top left). The zeroth-order approximation result, rescaled, is shown in the same figure (top right). The twin humps at the peaks of our prediction will be a generic prediction for any spherically symmetric galaxy cluster (non-mergers). The best-fitting MOG κ-model is shown in Fig. 14 (bottom left) along the line connecting the MOG centre to the main cluster κ-map peak. We show a 3D visualization of the full convergence κ-map model in the same figure (bottom right).

4.3 Including the galaxies

In considering the MOG κ-model resulting from the zeroth-order approximation, as shown in Fig. 14 (top right), it is tempting to try to explain the entire convergence κ-map by the X-ray gas mass, just by shifting the solid black line to the left by $\sim$200 kpc, but then there would be no way to explain the subcluster κ-map peak. We next proceed to account for the effect of the subcluster on the dimensionless gravitational coupling, $\mathcal{G}(r)$, of MOG, as shown in the best-fitting κ-model of Fig. 14 (bottom). Remarkably, as the MOG centre is separated from the main cluster Σ-map peak, say due to the gravitational effect of the subcluster, the centroid naturally shifts towards the κ-map peak, and the predicted height of the κ-map drops. Let us take the difference between the κ-map data and our best-fitting κ-model, to see if there is any 'missing mass'. We hypothesize that the difference can be explained by including the galaxies,

$$\kappa(x, y) = \frac{\bar{\Sigma}(x, y) + \bar{\Sigma}_{\rm galax}(x, y)}{\Sigma_{\rm c}}, \tag{77}$$

where $\bar{\Sigma}$ is the weighted surface mass density of equation (42), and the best-fitting κ-model of $\bar{\Sigma}/\Sigma_{\rm c}$ is derived from equations (41) and (42). Therefore, the galaxies contribute a 'measurable' surface mass density,

$$\Sigma_{\rm galax}(x, y) \approx \frac{\kappa(x, y)\Sigma_{\rm c} - \bar{\Sigma}(x, y)}{\mathcal{G}(x, y)}, \tag{78}$$

where $\mathcal{G}(x, y)$ corresponds to the best-fitting model of equation (18) listed in Table 3. The result of the galaxy subtraction of equation (78) is shown in Fig. 13. Now we may interpret Fig. 14 (bottom right) as the total convergence κ-map where the black surface is the contribution from the weighted surface density of the ICM gas, $\bar{\Sigma}/\Sigma_{\rm c}$, and the red surface is the remainder of the κ-map due to the contribution of the weighted surface density of the galaxies, $\bar{\Sigma}_{\rm galax}/\Sigma_{\rm c}$. We may calculate the total mass of the galaxies,

$$M_{\rm galax} = \int \Sigma_{\rm galax}(x', y')\mathrm{d}x'\,\mathrm{d}y'. \tag{79}$$

We were able to perform the integration within a 100 kpc radius aperture about the main cluster CD and subcluster BCG, separately, the results of which are listed in Table 5, where they are compared with the upper limits on galaxy masses set by *HST* observations. If the hypothesis that the predicted $M_{\rm galax}$ is below the bound set by *HST* observations is true, then it follows that

$$M_{\rm bary} = M_{\rm gas} + M_{\rm galax} \tag{80}$$

requires no addition of non-baryonic dark matter. The results of our best fit for $M_{\rm gas}$, $M_{\rm galax}$ and $M_{\rm bary}$ of equation (80) are listed in Table 5.

4.4 Dark matter

From the alternative point of view, dark matter is hypothesized to account for all of the 'missing mass' which results in applying Newton/Einstein gravity. This means, for the 2006 November 15 data release (Clowe et al. 2006a,b,c; Bradač et al. 2006), that the 'detected'

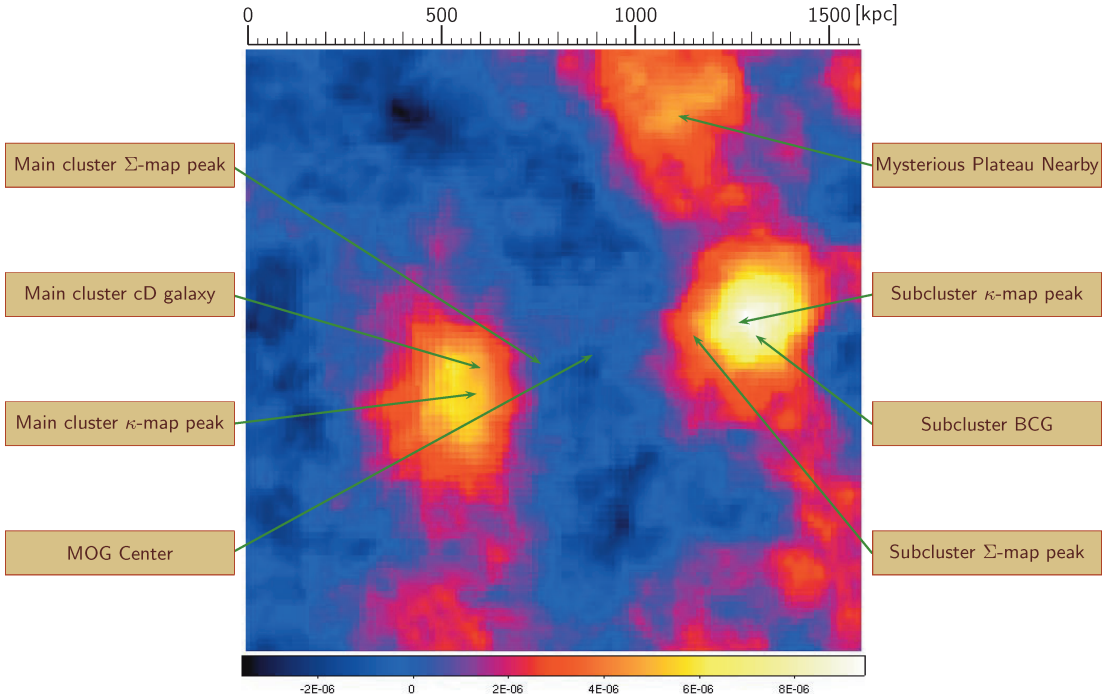

Figure 13. The galaxy surface density Σ-map prediction. The prediction of the Σ-map due to the galaxies as computed by the difference between the κ-map and our MOG κ-model, scaled as surface mass density according to equation (78). Σ-map and κ-map observed peaks are shown for comparison. The CD galaxy of the main cluster, the BCG of the subcluster and the MOG predicted gravitational centre are shown. J2000 and map (x, y) coordinates are listed in Table 1. Component masses (integrated within a 100 kpc radius aperture) for the main and subcluster, the MOG centre and the total predicted baryonic mass, $M_{\rm bary}$, for the Bullet Cluster 1E0657-558 are shown in Table 5.

dark matter must contribute a surface mass density,

$$\Sigma_{\rm DM}(x, y) \approx \kappa(x, y)\Sigma_{\rm c} - \Sigma(x, y), \tag{81}$$

with an associated total mass,

$$M_{\rm DM} = \int \Sigma_{\rm DM}(x', y')\mathrm{d}x'\,\mathrm{d}y'. \tag{82}$$

The integral of equation (82) becomes trivial on substitution of equation (81):

$$M_{\rm DM} = \Sigma_{\rm c} \int \kappa(x', y')\,\mathrm{d}x'\,\mathrm{d}y' - \int \Sigma(x', y')\,\mathrm{d}x'\,\mathrm{d}y', \tag{83}$$

where we have neglected $M_{\rm galax}$ in equation (83) because as is usually argued, the contribution from the galaxies in the dark matter paradigm is $\leqslant$ 1– 4 per cent of $M_{\rm total}$. The calculation of $M_{\rm DM}$ in equation (83) was performed by a pixel-by-pixel sum over the convergence κ-map data and surface density Σ-map data, within a 100 kpc radius aperture around the main and subcluster κ-map peaks, respectively. The result of our computation is included in Table 5.

We emphasize, here, that for each of the main cluster, subcluster and total Σ-map, our results of Table 5 indicate that

$$M_{\rm bary} = M_{\rm gas} + M_{\rm galax} \ll M_{\rm DM} \tag{84}$$

implying that we have successfully put Bullet Cluster 1E0657-558 on a lean diet! This seems to us to be a proper use of *Occam's razor*. The mass ratios, $M_{\rm galax}/M_{\rm gas}$, for the main and subcluster and central ICM are shown at the bottom of Table 5. The result of $M_{\rm galax}/M_{\rm gas} \approx 0.4$ per cent in the central ICM is due to the excellent fit in MOG across the hundreds of kpc separating the main and subcluster. The dark matter result of $M_{\rm gas}/M_{\rm DM} \approx 45$ per cent in the central ICM implies that the evolutionary scenario does not lead to a spatial dissociation between the dark matter and the ICM gas, which indicates that the merger is ongoing. In contrast, the MOG result shows a true dissociation between the galaxies and the ICM gas as required by the evolutionary scenario. The baryon-to-dark matter fraction over the full Σ-map is 32 per cent, which is significantly higher than the ΛCDM cosmological baryon mass fraction of $17^{+1.9}_{-1.2}$ per cent (Spergel et al. 2006). The distribution of mass predicted by MOG versus the dark matter paradigm is shown in Fig. 15.

5 CONCLUSIONS

The MOG theory provides a fit to the κ-map of the 2006 November 15 data release (Clowe et al. 2006c). The model, derived purely from the X-ray imaging Σ-map observations combined with the galaxy Σ-map predicted by MOG, accounts for the κ-map peak amplitudes and their spatial dissociation without the introduction of non-baryonic dark matter.

The question of the internal degrees of freedom in MOG has to be further investigated. It would be desirable to derive a theoretical prediction from the MOG field equations that fit the empirically determined mass and distance scales in Fig. 6.

It could be argued that any modified theory designed to solve the dark matter conundrum, such as MOND or MOG, has less freedom than dark matter. So, the important question to resolve is precisely how much freedom the MOG solution has. On one hand we said, definitely, that there was no freedom in choosing the pair of M_0 and r_0 for the main cluster since it was well described by an isothermal sphere, to an excellent approximation. We further argued that the subcluster was (per mass) a small perturbation to the ICM. But if MOG has more freedom than MOND, but less freedom than dark

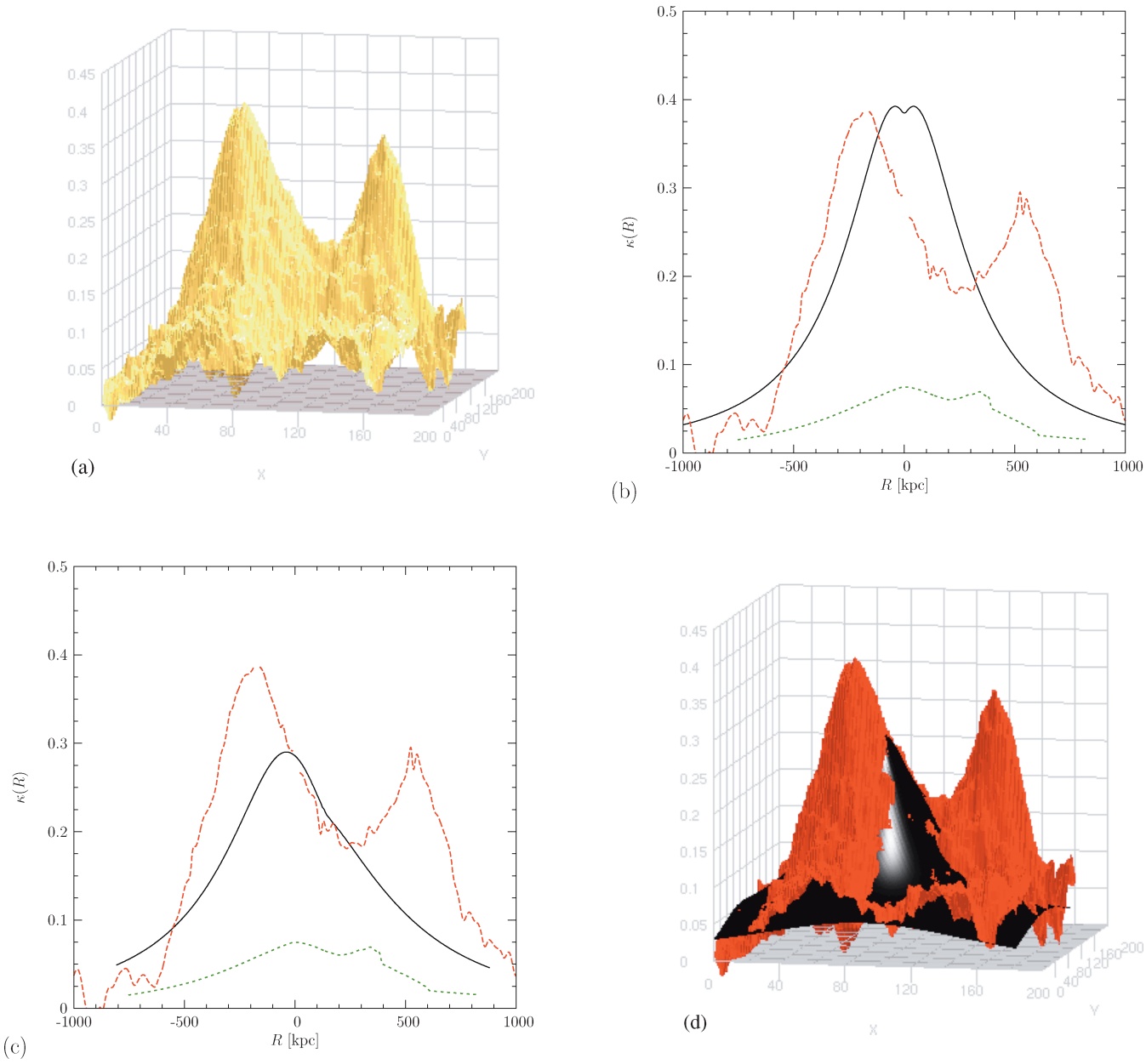

Figure 14. The convergence κ-map 2006 November 15 data release (Clowe et al. 2006c) and our κ-models. The convergence κ-map 2006 November 15 data release (Clowe et al. 2006c) is shown in (a) and in red in (b)–(d). The best-fitting MOG κ-model due to the main-cluster ICM gas is shown in solid black. (b) The zeroth-order approximation and (c and d) the best-fitting MOG prediction. The difference between the red curve (total convergence, κ, due to all baryons) and the black curve (convergence, κ due to the ICM gas) is taken to be the contribution of the galaxies in the absence of dark matter. The galaxy result is shown in Figs 13 and 15. The scaled Σ-map $\Sigma(x, y)/\Sigma_c$ data are shown in short-dashed green in Figs (c) and (d), and also in Fig. 4.

Table 5. Summary of component mass predictions. Component masses (integrated within a 100 kpc radius aperture) for the main and subcluster and the MOG centre. The total predicted mass for the Bullet Cluster 1E0657-558 is integrated over the full Σ-map.

Component	Main cluster	Subcluster	Central ICM	Total
$M_{\rm gas}$	$7.0 \times 10^{12}\,{\rm M}_\odot$	$5.8 \times 10^{12}\,{\rm M}_\odot$	$6.3 \times 10^{12}\,{\rm M}_\odot$	$2.2 \times 10^{14}\,{\rm M}_\odot$
$M_{\rm galax}$	$1.8 \times 10^{12}\,{\rm M}_\odot$	$3.1 \times 10^{12}\,{\rm M}_\odot$	$2.4 \times 10^{10}\,{\rm M}_\odot$	$3.8 \times 10^{13}\,{\rm M}_\odot$
$M_{\rm bary}$	$8.8 \times 10^{12}\,{\rm M}_\odot$	$9.0 \times 10^{12}\,{\rm M}_\odot$	$4.9 \times 10^{12}\,{\rm M}_\odot$	$2.6 \times 10^{14}\,{\rm M}_\odot$
$M_{\rm DM}$	$2.1 \times 10^{13}\,{\rm M}_\odot$	$1.7 \times 10^{13}\,{\rm M}_\odot$	$1.4 \times 10^{13}\,{\rm M}_\odot$	$6.8 \times 10^{14}\,{\rm M}_\odot$
$M_{\rm galax}/M_{\rm gas}$	26 per cent	53 per cent	0.4 per cent	17 per cent
$M_{\rm gas}/M_{\rm DM}$	33 per cent	34 per cent	45 per cent	32 per cent

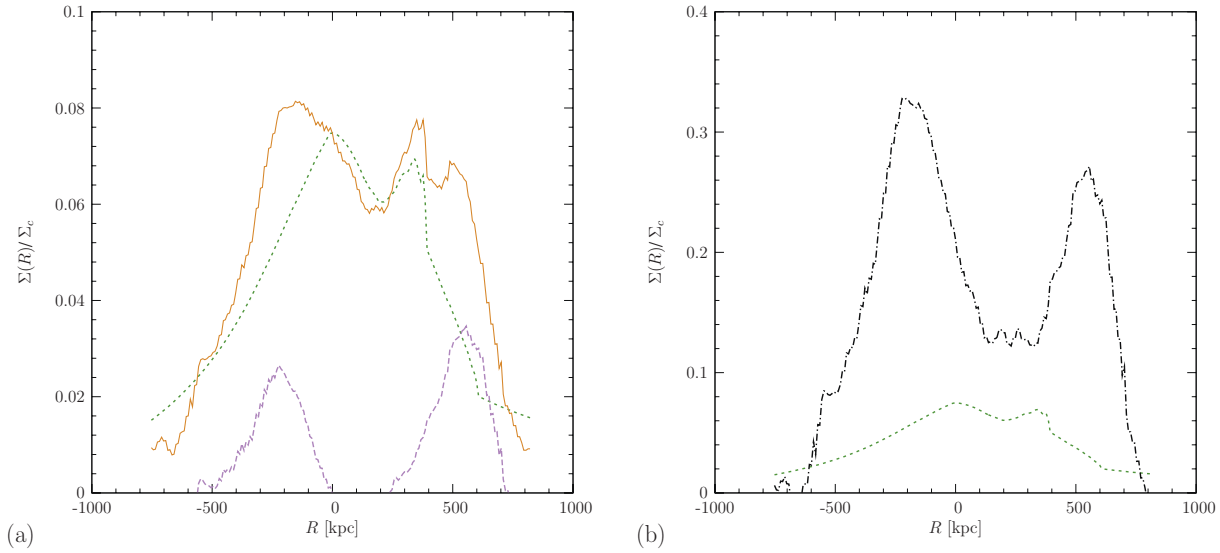

Figure 15. Plot of the scaled surface density Σ/Σ_c along the line connecting the main cluster Σ-map peak with the main CD. (a) The scaled surface density for the MOG predicted galaxies, Σ_{galax}/Σ_c and the MOG predicted visible baryons, Σ_{bary}/Σ_c, compared to the ICM gas. (b) The scaled surface density of dark matter, Σ_{DM}/Σ_c, compared to ICM gas. The prediction of equation (78) for the galaxies is shown in long-dashed magenta, and the prediction of equation (80) for the visible baryonic mass is shown in solid brown. The calculation of equation (81) for dark matter is shown (right-hand side) in dash–dotted black. The ICM gas distribution inferred from the Σ-map data is shown in short-dashed green on each plot.

matter, then what is the additional degree of freedom that enters the Bullet Cluster observations? The question is resolved in that there is a physical degree of freedom due to a lack of spherical symmetry in the Bullet Cluster, and whence the galaxies sped outward, beyond the ICM gas clouds which lagged behind – effectively allowing the galaxies to climb out of the spherical minimum of the Newtonian core where MOG effects are small (inside the MOG range r_0) upwards along the divergence of the stress-energy tensor (Newtonian potential, if you prefer a simple choice) towards the far-IR region of large gravitational coupling, G_∞.

In fact, the Bullet Cluster data results describe, to a remarkable precision, a simple King β-Model. Our analysis, with the result to the best fit shown in Table 2, uniquely determines the mass profile $\rho(r)$ of equation (21) used throughout our computations. We permitted only a single further degree of freedom to account for the fits of Figs 14 and the predictions of Figs 13 and 15; this was the location of the MOG centre, where the gravitational coupling, $\mathcal{G}(0) \to 1$, is a minimum at the Newtonian core. Remarkably, the data did not permit a vanishing MOG centre, with respect to the peak of the ICM gas $\rho(0)$. We have shown the location of the MOG centre as determined by a numerical simulation of convergence map according to equations (41) and (42) in each of Figs 3, 10, 12 and 13 and provided the coordinates in Table 1.

The surface density Σ-map derived from X-ray imaging observations is separable into the main cluster and the subcluster-subtracted surface density Σ-map through a low χ^2-fitting King β-model. Following the (>100) galaxy cluster survey of Brownstein & Moffat (2006b), we have derived a parameter-free (unique) prediction for the X-ray temperature of the Bullet Cluster 1E0657-558 which has already been experimentally confirmed. In equations (41) and (42), we have derived a weighted surface mass density, $\tilde{\Sigma}$, from the convergence κ-map which produced a best-fitting model (bottom of Fig. 14 and Table 3). We have computed the dark matter and the MOG predicted galaxies and baryons (Fig. 15), and noted the tremendous predictive power of MOG as a means of utilizing strong and weak gravitational lensing to do galactic photometry – a powerful tool simply not provided by any candidate dark matter (Fig. 13). The predictions for galaxy photometry will be the subject of future investigations in MOG, and the availability of weak and strong gravitational lensing surveys will prove invaluable in the future.

Although dark matter allows us to continue to use Einstein (weak field) and Newtonian gravity theory, these theories may be misleading at astrophysical scales. By searching for dark matter, we may have arrived at a means to answer one of the most fundamental questions remaining in astrophysics and cosmology: how much matter (energy) is there in the Universe and how is it distributed? For the Bullet Cluster 1E0657-558, dark matter dominance is a ready answer, but in MOG we must answer the question with only the visible contribution of galaxies, ICM gas and gravity.

ACKNOWLEDGMENTS

This work was supported by the Natural Sciences and Engineering Research Council of Canada (NSERC). We thank Douglas Clowe and Scott Randall for providing early releases of the gravitational lensing convergence data and X-ray surface mass density data, respectively, and for stimulating and helpful discussions. Research at Perimeter Institute for Theoretical Physics is supported in part by the Government of Canada through NSERC and by the Province of Ontario through the Ministry of Research and Innovation (MRI).

REFERENCES

Aguirre A., Schaye J., Quataert E., 2001, ApJ, 561, 550
Angus G. W., Famaey B., Zhao H. S., 2006, MNRAS, 371, 138
Angus G. W., Shan H. Y., Zhao H. S., Famaey B., 2007, ApJ, 654, L13
Bekenstein J. D., 2004, Phys. Rev. D, 70, 083509
Bradač M. et al., 2006, ApJ, 652, 937
Brownstein J. R., Moffat J. W., 2006a, ApJ, 636, 721
Brownstein J. R., Moffat J. W., 2006b, MNRAS, 367, 527
Brownstein J. R., Moffat J. W., 2006c, Class. Quantum Grav., 23, 3427
Cavaliere A. L., Fusco-Femiano R., 1976, A&A, 49

Chandrasekhar S., 1960, Principles of Stellar Dynamics. Dover, New York
Clowe D., Gonzalez A., Markevitch M., 2004, ApJ, 604, 596
Clowe D., Bradač M., Gonzalez A. H., Markevitch M., Randall S. W., Jones C., Zaritsky D., 2006a, ApJ, 648, L109
Clowe D., Randall S. W., Markevitch M., 2006b, preprint (arXiv:astro-ph/0611496)
Clowe D., Randall S. W., Markevitch M., 2006c, http://flamingos.astro.ufl.edu/1e0657/index.html
King I. R., 1966, AJ, 71, 64
Markevitch M., 2006, in Wilson A., ed., ESA SP-604: The X-ray Universe 2005 Chandra Observation of the Most Interesting Cluster in the Universe. ESA, Noordwijk, p. 723
Markevitch M., Gonzalez A. H., David L., Vikhlinin A., Murray S., Forman W., Jones C., Tucker W., 2002, ApJ, 567, L27
Milgrom M., 1983, ApJ, 270, 365
Moffat J. W., 2005, J. Cosmo. Astropart. Phys., 05, 003
Moffat J. W., 2006a, J. Cosmo. Astropart. Phys., 03, 004
Moffat J. W., 2006b, preprint (arXiv:astro-ph/0608675)
Moffat J. W., 2007, Int. J. Mod. Phys. D, in press
Nieto M. M., Anderson J. D., 2005, Class. Quantum Grav., 22, 5343
Oort J., 1932, Bull. Astron. Inst. Netherlands, 6, 249
Peacock J. A., 2003, Cosmological Physics. Cambridge University Press, Cambridge, UK
Pointecouteau E., Silk J., 2005, MNRAS, 364, 654
Reiprich T. H., 2001, PhD thesis, Ludwig-Maximilians Univ.
Reiprich T. H., Böhringer H., 2002, ApJ, 567, 716
Reuter M., Weyer H., 2006, Int. J. Mod. Phys. D, 15, 2011
Sanders R. H., 2006, MNRAS, 370, 1519
Sanders R. H., McGaugh S. S., 2002, ARA&A, 40, 263
Spergel D. N., Bean R., Dore' O., Nolta M. R., Bennett C. L., Hinshaw G., Jarosik N., Komatsu E. E. A., 2007, ApJS, 170, 377
Takahashi R., Chiba T., 2007, ApJ, in press
Zwicky F., 1933, Helv. Phys. Acta, 6, 110

This paper has been typeset from a TEX/LATEX file prepared by the author.